

AGN-Host Galaxy Connection: Morphology and Colours of X-ray Selected AGN at $z \leq 2$

M. Pović^{1,2,3,*}, M. Sánchez-Portal^{4,5,**}, A. M. Pérez García^{1,6,5}, A. Bongiovanni^{1,6,5}, J. Cepa^{5,1}, M. Huertas-Company^{7,8}, M. A. Lara-López^{1,9}, M. Fernández Lorenzo^{1,3}, A. Ederoclite^{1,10}, E. Alfaro³, H. Castañeda¹¹, J. Gallego¹², J. I. González-Serrano¹³, and J. J. González¹⁴

¹ Instituto de Astrofísica de Canarias (IAC), La Laguna, Tenerife, Spain

² Astrophysics and Cosmology Research Unit (ACRU), School of Mathematical Sciences, University of Kwa-Zulu Natal (UKZN), Durban, South Africa

³ Instituto de Astrofísica de Andalucía (IAA), Granada, Spain

⁴ Herschel Science Centre (HSC), European Space Agency Centre (ESAC)/INSA, Villanueva de la Cañada, Madrid, Spain

⁵ Asociación ASPID, Apartado de Correos 412, La Laguna, Tenerife, Spain

⁶ Departamento de Astrofísica, Universidad de La Laguna (ULL), La Laguna, Tenerife, Spain

⁷ GEPI, Paris-Meudon Observatory, Meudon, France

⁸ University of Paris, Paris, France

⁹ Australian Astronomical Observatory (AAO), Sidney, Australia

¹⁰ Centro de Estudios de Física del Cosmos de Aragón (CEFCA), Teruel, Spain

¹¹ Escuela Superior de Física y Matemáticas, Instituto Politécnico Nacional (IPN), Mexico D.F, Mexico

¹² Departamento de Astrofísica y CC. de la Atmósfera, Universidad Complutense de Madrid, Madrid, Spain

¹³ Instituto de Física de Cantabria, CSIC-Universidad de Cantabria, Santander, Spain

¹⁴ Instituto de Astronomía UNAM, México D.F, México

Preprint online version: October 10, 2018

ABSTRACT

Context. The connection between AGN and their host galaxies has been widely studied over recent years, showing it to be of great importance for providing answers to some fundamental questions related with AGN fuelling mechanisms, their formation and evolution.

Aims. Using X-ray and one of the deepest broad-band optical data sets, morphology and colours have been studied in relationship with X-ray properties for sources at redshifts $z \leq 2.0$, using a sample of 262 AGN in the Subaru/XMM-Newton Deep Survey (SXDS).

Methods. Morphological classification has been obtained using the new galSVM code. Colour-magnitude diagrams have been studied in relationship with redshift, morphology, X-ray obscuration, and X-ray-to-optical flux ratio. The significance of different regions has been analysed on colour-magnitude diagrams, relating the observed properties of AGN populations with some models of their formation and evolution.

Results. Our morphological classification suggests that different mechanisms may be responsible for triggering the nuclear activity in galaxies. Observing populations of X-ray detected AGN on both colour-magnitude and colour-stellar mass diagrams, the highest number of sources is found to reside in the green valley at redshifts $\approx 0.5 - 1.5$. However, a higher number of low luminosity AGN has been detected in comparison with previous works due to the high depth of the SXDS optical data. Whether AGN are being hosted by early- or late-type galaxies, no clear relationship has been found with the optical colours (independently of redshift), as typical for normal galaxies. Both early- and late-type AGN cover similar ranges of X-ray obscuration, with both unobscured and obscured sources.

Conclusions. Our findings may confirm some previous suggestions, that X-ray selected AGN residing in the green valley present a transition population, quenching star formation through different AGN feedback mechanisms and evolving to red sequence galaxies. They might be hosted by similar sources (majority of sources being late-type elliptical and lenticular galaxies, and early-type spirals), having similar stellar populations, being triggered mainly through major and/or minor mergers, and in some cases through some secular mechanism, as shown in previous numerical simulations. In the mentioned transition we observe different phases of AGN activity, with some AGN being in the 'QSO-mode': detected as compact, blue, and unobscured in X-rays, and with others passing through different phases before and after the 'QSO-mode', being obscured and unobscured in X-rays, respectively.

Key words. Galaxies: active – Galaxies: fundamental parameters – Galaxies: distances and redshifts – Galaxies: structure – X-rays: galaxies

1. Introduction

Active Galactic Nuclei (AGN) play an important role in many aspects of modern cosmology, and of particular interest is the is-

sue of the interplay between AGN and their host galaxies. The study of AGN host galaxies is shown to be of great importance for providing answers to some still unanswered questions. These questions include the effect of the AGN on their host galaxy and vice-versa, the origin of the accretion material, the triggering mechanisms that initiate the active phase in a galaxy, the du-

* email: mpovic@iaa.es

** email: miguel.sanchez@sciops.esa.int

ration of the active phase, etc., therefore putting important constraints on the models of supermassive black hole (SMBH) formation and growth, as well as the formation and evolution of galaxies.

Over recent years, fundamental relationships between the AGN and host galaxy properties have been suggested, particularly with their bulges, showing the connection between galaxy formation and AGN activity. This involves the discoveries that most of the close massive galaxies have a SMBH in their centres (Magorrian et al. 1998), that local AGN predominantly reside in galaxies dominated by a massive bulge (Kauffmann et al. 2003), and that the masses of the central SMBHs in nearby galaxies correlate with several host bulge properties, including luminosity (Kormendy & Richstone 1995; McLure et al. 2000; Marconi & Hunt 2003), velocity dispersion (Ferrarese & Merritt 2000; Gebhardt et al. 2000), mass (Magorrian et al. 1998; Ferrarese 2004), and galaxy light concentration (Graham et al. 2001). Moreover, in a wide range of redshifts it has been obtained that early-type galaxies, having more massive black holes in their centres, have lower Eddington ratios compared with later-type galaxies (Hickox et al. 2009; Pović et al. 2009a,b).

Morphology and colours are two key elements used in order to study the properties of AGN host galaxies, their connection with AGN, and their evolution. They represent two of the most accessible indicators of the galaxy's physical structure, being crucial to understand the formation of galaxies throughout cosmic history and to provide answers to some of the fundamental questions mentioned above.

The morphological study of AGN host galaxies has been one of the active research fields over the past years, leading to the inconsistency between the results obtained when using samples at both low and high redshifts, and different methods of morphological classification. The first important morphological study of local AGN (mostly Seyfert galaxies) showed that most of them reside in spiral galaxies (e.g., Adams 1977; Heckman 1978; Ho, Filippenko, & Sargent 1995). However, Kauffmann et al. (2003) analysed thousands of low-redshift ($z \leq 0.4$) AGN host galaxies from the Sloan Digital Sky Survey (SDSS), and found that most AGN reside in massive galaxies, having distributions of sizes, stellar surfaces, mass densities, and concentrations, all similar to those of early-type SDSS galaxies. On the other hand, Choi et al. (2009) found that most AGN from the SDSS survey reside in late-type galaxies with intermediate luminosities and velocity dispersions. Deep surveys made it possible to study the morphological properties of intermediate- and high-redshift AGN host galaxies selected at different wavelengths (mainly X-ray, optical, IR, and radio). Most of these studies found that X-ray selected AGN usually reside in spheroid/bulge-dominated galaxies (e.g., Pierce et al. 2007; Pović et al. 2009a); however some studies found higher concentrations of later-types (Gabor et al. 2009).

Beside morphology, colours are also important to for revealing the nature of AGN host galaxies. It is well known from previous studies of colour-magnitude relations that, in general, normal galaxies may be located in the 'red sequence', populated by massive, bulge-dominated galaxies having older, passively evolving stellar populations, or in the 'blue cloud', populated by blue, star-forming galaxies of small and intermediate masses (e.g., Baldry et al. 2004; Weiner et al. 2005; Cirasuolo et al. 2005). In most (if not all) studies, galaxies hosting AGN lie predominantly in the 'green valley' of the colour-magnitude diagrams, a transition region located between the red sequence and the blue cloud (e.g., Barger et al. 2003; Sánchez et al. 2004;

Nandra et al. 2007; Georgakakis et al. 2008; Silverman et al. 2008; Treister et al. 2009). This has been considered as one of the pieces of evidence of a connection between AGN and galaxy evolution, suggesting that AGN feedback mechanism may play an important role in regulating (quenching) star formation, moving the galaxies from blue, star-forming to passive, red sequence galaxies (e.g., Springel et al. 2005; Schawinski et al. 2006; Hasinger 2008). Recently, Hickox et al. (2009) studied three populations of AGN, selected in radio, X-ray, and IR, and found that most radio selected AGN are hosted by red sequence galaxies, that X-ray selected AGN occupy all areas on the colour-magnitude diagram, but mostly the green valley, while most IR selected AGN reside in slightly bluer galaxies compared with the two previous populations. However, other results show that there is no strong evidence in AGN host galaxies for either highly suppressed star formation, which is expected if AGN are responsible for star formation quenching, or elevated star formation, when compared to galaxies of similar stellar masses and redshifts (Alonso-Herrero et al. 2008; Brusa et al. 2009).

As mentioned above, although many analyses have been carried out over the past few years in order to study the morphological and colour properties of AGN host galaxies, there are still many inconsistencies between the results obtained and their interpretation. Particularly, the interpretation of morphology still remains a problem in the framework of galaxy evolution. Since the quality of the measured morphology is strongly dependent on the image resolution, the morphological classification in deep surveys is still very difficult, especially when dealing with faint and high redshift sources. Therefore, additional studies are necessary using deep observations for obtaining large samples of AGN, and testing new methods for morphological classification, in order to reveal the nature of AGN host galaxies, their connection with AGN, and to study their evolution throughout cosmic time.

In this work we perform a study of the morphological and colour properties of a sample of 262 X-ray detected AGN at redshifts $z \leq 2$ in the Subaru/XMM-Newton Deep Survey (SXDS; Furusawa et al. 2008) field, using one of the deepest optical datasets available to the astronomical community. Morphological classification has been obtained using gaSVM (Huertas-Company et al. 2008, 2009), one of the new codes especially useful for analysing morphology when dealing with low spatial resolution and high redshift data. A set of different morphological parameters has been studied, and an additional visual classification has been performed as well. The evolution of the AGN host galaxies on the colour-magnitude diagrams has been studied in four redshift intervals (up to $z \leq 2$ with bins of 0.5), for different morphological and X-ray types, and for objects having different X-ray-to-optical (X/O) flux ratio. Different regions on the colour-magnitude diagrams have been analysed, relating the observed AGN properties in each region with some current models of AGN formation and evolution. Finally, this paper provides the scientific community with a catalogue of a large sample of AGN detected in the SXDS field, including their photometric X-ray and optical data, morphological properties, rest-frame colours, and redshifts. The catalogue can be used in further studies related with AGN populations. This paper is part of the preparatory work for the long-term OTELO¹ survey (Cepa et al. 2008). OTELO is an on-going emission line survey

¹ OSIRIS Tunable Emission Line Object survey

using the Tunable Filters of OSIRIS² at the GTC³ telescope. The survey aims for performing a narrow-band tomography over a 21nm window centered at 920nm in at least two selected fields, and its science cases include the study of SFR density and chemical evolution in the Universe, high redshift QSO and AGN at any redshift, emission line ellipticals and Galactic emission line stars (Cepa et al. 2007; Pović et al. 2009a; Cepa et al. 2011; Lara-López et al. 2011).

The paper is structured as follows: in Section 2, we describe the observational data used in this work, including a brief summary of the X-ray data processing and source detection, optical broad-band data, selection of X-ray emitters with optical counterparts, and estimation of the k-corrections and photometric redshifts. Section 3 describes the morphological classification of X-ray selected AGN. All analysis related with AGN colours is described in Section 4, being considered in relation with redshift, morphology, X-ray obscuration, and X/O flux ratio, comparing the obtained results with some models of AGN formation and evolution. Finally, Section 5 summarises the main results obtained in this work. The concordance cosmology with $\Omega_\Lambda = 0.7$, $\Omega_M = 0.3$, and $H_0 = 70 \text{ km s}^{-1} \text{ Mpc}^{-1}$ is assumed. Unless otherwise specified, all magnitudes are given in the AB system.

The catalogue presenting the data obtained in this work is described in the Appendix and presented in the electronic edition.

2. Observational material and data reduction

The Subaru/XMM-Newton Deep Survey (SXDS; Sekiguchi et al. 2010, in prep.) is a large survey, covering a contiguous region of > 1 square degree centred at RA = $02^h 18^m$ and DEC = $-05^\circ 00'$, with limiting AB magnitude at 3σ of 28.4 in the B band, and with the typical seeing of 0.8 (Furusawa et al. 2008). The SXDS field has been observed at different wavelengths, from X-rays to radio. We briefly describe the data sets used in this work below. X-ray and optical broad-band data (Pović et al. 2009b; Furusawa et al. 2008) are the main data used in our analysis in order to detect and select the AGN populations, and to derive their nuclear and morphological properties. Additionally, near- and mid-IR data have been used in order to measure k-corrections and photometric redshifts.

2.1. X-ray data

The SXDS was observed by XMM-Newton during the years 2000, 2002, and 2003 (PI Michael G. Watson). Seven pointings were obtained in the 0.2–10 keV energy range. The central observation is the deepest one, with a nominal exposure time of ~ 100 ksec, being surrounded by six shallower observations, each of them with an exposure time of ≈ 50 ksec. The surveyed area is $\approx 1.14 \text{ deg}^2$, covering the complete region of 5 mosaic, optical images taken with the Subaru telescope (see below).

The required data have been gathered from the XMM-Newton v.5.0 scientific archive (XSA⁴). Data processing was carried out by means of the Science Analysis System (SAS⁵) v7.1.2 package, using the latest relevant Current Calibration Files (CCF). The raw Observation Data Files (ODF) were

processed using the standard SAS tasks *emproc* (for MOS cameras) and *epproc* (for pn camera) to produce calibrated event lists. Light curves were obtained by means of *xmmselect* and *OGIP light curve* tasks, selecting only events with pattern 0-4 (single and double) and PI 200-12000 for the pn camera, and pattern 0-12 and PI 200-15000 for the MOS cameras. Good Time Intervals (GTIs) were created using the *tabingen* task, filtering event lists with RATE parameter. To merge event lists and additional files we used *merge* task. Six energy bands were selected, as shown in Table 1. Moreover, combining soft and hard bands we obtained fluxes in the 0.5 - 4.5 keV energy range. This band is the most used in our analysis for comparing our results with previous ones. Figure 1 shows the distribution of fluxes in five energy bands, for all detected X-ray sources, and for 262 sources analysed in this paper (see Section 2.6). The *evselect* task was used to produce the images and *fits* files in all selected energy ranges, separately for each instrument, and selecting only events with FLAG=0. We have computed the survey area as a function of the completeness flux in the total band (see Figure 2) by evaluating the histogram of the survey distribution for increasing area values. The completeness flux for that area is derived as the energy bin corresponding to the maximum of the histogram. The survey is complete at $f_{0.5-10\text{keV}} \approx 3.6 \times 10^{-15} \text{ erg cm}^{-2} \text{ s}^{-1}$ for the maximum survey area, $\sim 1.4 \text{ deg}^2$.

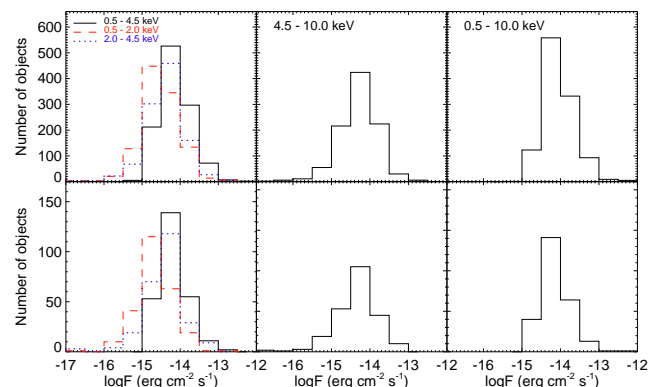


Fig. 1. X-ray flux distributions for all 1121 X-ray detected sources (Top) and for 262 objects with $z \leq 2.0$ analysed in this paper (Bottom; see Section 2.6). Flux distributions are represented in the 0.5 - 2.0 (dashed red line), 2.0 - 4.5 (dotted blue line), and 0.5 - 4.5 keV (solid black line) energy bands (left panels), 4.5 - 10.0 keV (middle panels), and 0.5 - 10.0 keV range (right panels).

Source detection was performed by means of the *edetect_chain* SAS procedure. To minimize the number of spurious detections the likelihood threshold parameter⁶ was set at $L = 14$. Thus the probability that the source exists is at least $P = 0.9999916847$, or less than one fake source per instrument, per pointing, and per band. In order to convert count rates to energy fluxes we computed energy conversion factors (ecf) using PIMMS (Mukai, 1993), using power law function with a

⁶ $L = -\ln(1 - P)$, where P is the probability to have a spurious detection due to random Poisson fluctuations

² Optical System for Imaging and low Resolution Integrated Spectroscopy

³ Gran Telescopio de Canarias; <http://www.gtc.iac.es/>

⁴ <http://xmm.esac.esa.int/xsa/>

⁵ http://xmm.esac.esa.int/external/xmm_data_analysis

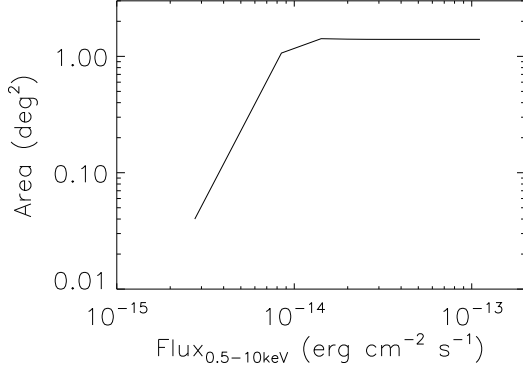


Fig. 2. Survey area as a function of flux in the total (0.5–10 keV) band.

spectral index $\Gamma=1.8$ (e.g., Mateos et al. 2005), and a galactic absorption $nH=2.5 \times 10^{20} \text{ cm}^{-2}$ (Dickey & Lockman 1990). PIMMS measured all XMM-Newton ecf values using the aperture of 15 arcsec, and ecf values had to be multiplied by a factor of 1.47 (aperture correction) in order to obtain good superposition with the XMM-Newton PSF and to integrate the flux of the source to the large distances (Saxton, R. priv. comm. and XMM-Newton team for more information). The number of sources in each energy band, final ecf values, and median and limiting fluxes are listed in Table 1 for each energy range. Hardness ratios⁷ have been also defined. We have used $HR(\text{hard}/\text{soft}) \equiv HR(2 - 4.5 \text{ keV}/0.5 - 2 \text{ keV})$ in this work.

Source detection has been performed separately in each field, and for each instrument. Double detections have been eliminated from the overlapping regions, removing detections with shorter exposure time from the source lists. Finally, source files obtained for each instrument have been cross-matched, creating therefore only one file, keeping only detections with $S/N > 2$ in the total 0.5-10.0 keV range. The final catalogue has 1121 unique X-ray emitters, including sources detected in at least one of six energy bands.

2.1.1. Comparison with Ueda et al. results

Ueda et al. (2008) recently published a catalogue of X-ray emitters in the SXDS field. A total catalogue consists of 1245 X-ray sources detected in one of six selected energy bands: 0.3-0.5 keV (ultrasoft), 0.5-2 keV (soft), 2-4.5 keV (medium), 4.5-10 keV (ultrahard), 0.5-4.5 keV (XID), or 2-10 keV (hard). The data in the first four bands are publicly available. In general, the data reductions carried out in Ueda et al. (2008) and our works are quite similar. However, there are two main differences related with the source detection. First, Ueda et al. (2008) performed the source detection to the summed pn and MOS images, while we used individual images and finally summed detections from each camera, as explained above. Second, Ueda et al. (2008) adopted a detection likelihood threshold of 7 in a single band, while we used a more restrictive value, accepting only sources detected with a maximum likelihood above 14, and keeping only detections with $S/N > 2$ in the total

⁷ Defined as: $HR(\Delta_1 E/\Delta_2 E) = \frac{CR(\Delta_1 E) - CR(\Delta_2 E)}{CR(\Delta_1 E) + CR(\Delta_2 E)}$, where $\Delta_1 E$ y $\Delta_2 E$ are different energy bands and $CR(\Delta_n E)$ is the count rate in a given energy band

0.5-10.0 keV range.

Figure 3 shows $\log N - \log S$ relations in soft (0.5-2 keV) and total (0.5-10 keV) bands, where the total band for Ueda et al. (2008) data presents the sum of information obtained in their soft, medium and ultrahard bands. Although in the soft band the Ueda et al. (2008) data are more sensitive, our X-ray emitters with optical counterparts are in good correlation with the whole Ueda et al. (2008) sample. However, a higher density of sources has been detected in our full sample, probably due to the differences between source detection procedures explained above. On the other hand, limiting fluxes are in good correlation in the total band, and a higher density of sources has been detected in the Ueda et al. (2008) work, in comparison with both our full sample and optical counterparts, probably due to the less sensitive detection threshold used by the authors.

Using a cross-matched radius of 5 arcsec, 857 counterparts (808 unique ones) have been found between Ueda et al. (2008) and our catalogues. Sources contained in the Ueda et al. (2008) catalogue that are missing in ours are in general fainter (e.g., around 90% of these objects have fluxes below our limiting flux in the soft band). On the other hand, sources contained in our catalogue but not contained in the Ueda et al. (2008) catalogue are in general at lower S/N ratios (e.g., $\sim 50\%$ and $\sim 75\%$ of objects have S/N ratios between 2-3 and 2-4, respectively). Good correlation has been found for all counterparts between fluxes, with the linear correlation coefficients of 0.99, 0.97, 0.93, 0.96, and 0.99 in the 0.5-2 keV, 2-4.5 keV, 4.5-10 keV, 0.5-10 keV, and 0.5-4.5 keV bands, respectively, where the correlation coefficient of 1.0 presents a perfect linear correlation. In the soft band the Ueda et al. (2008) data are more sensitive, as mentioned above, while in the ultrahard and total bands limiting fluxes are in a good agreement. We are not able to provide the comparison between our and Ueda et al. (2008) X-ray luminosities, since they were not measured by the authors.

2.2. Optical data

Optical imaging observations were carried out with the Suprime-Cam installed at the Subaru Telescope at Mauna Kea (Furusawa et al. 2008). Five continuous sub-fields were observed, covering an area of 1.22 deg^2 with a total integration time of 133 hours. Each sub-field corresponds to a single Suprime-Cam field of view $\sim 34' \times 27'$, in five broad-band filters B, V, R_c , i' , and z' , with limiting AB magnitudes at 3σ of: 28.4, 27.8, 27.7, 27.7, and 26.6, respectively. Publicly available catalogues have been downloaded from the SXDS web page⁸, each of them containing 5-band aperture photometry (performed through fixed 2 and 3 arcsec apertures). The total number of objects are: 940,853, 1,002,561, 901,094, 899,484, and 842,590, in the B, V, R_c , i' , and z' bands, respectively.

2.3. Near-IR data

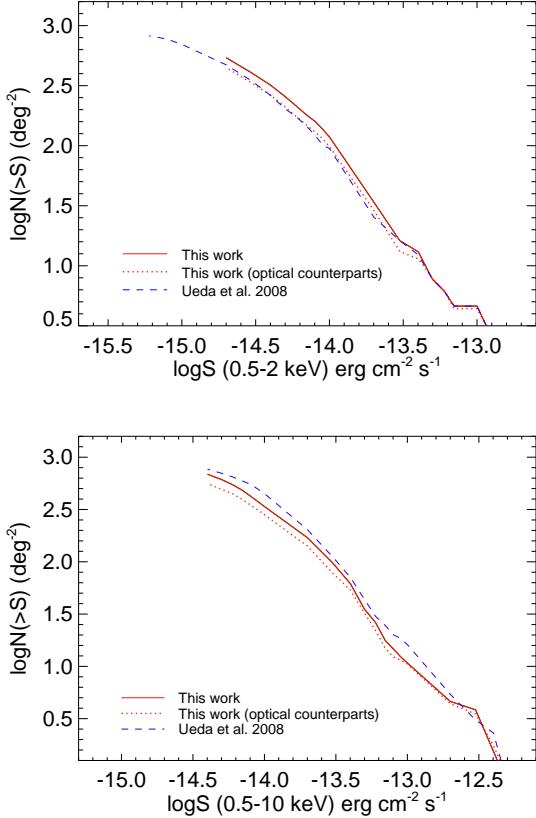
We have used near-IR (NIR) data from the XMM-LSS survey (that encompasses the SXDS field), being part of the United Kingdom IR Telescope Deep Sky Survey (UKIDSS). Specifically, we have downloaded and used the UKIDSS JHK Second Data Release (DR2) catalogue⁹. The photometric system is described in Hewett et al. (2006), and the calibration is

⁸ <http://www.naoj.org/Science/SubaruProject/SXDS/index.html>

⁹ <http://www.ukidss.org/archive/archive.html>; Warren et al. (2007)

Table 1. Selected energy bands, number of detected sources in each band, computed energy conversion factors, and flux properties of X-ray emitters in the SXDS field

Band	Energy range (keV)	Num. of sources	MOS ecf (10^{11} ct erg $^{-1}$ cm 2)	<i>pn</i> ecf (10^{11} ct erg $^{-1}$ cm 2)	Median flux (10^{-15} erg cm $^{-2}$ s $^{-1}$)	Limiting flux (10^{-15} erg cm $^{-2}$ s $^{-1}$)
soft	0.5-2.0	1103	2.102	5.977	2.84	2.25
hard	2.0-4.5	1048	0.786	1.41	4.37	4.0
veryhard	4.5-10.0	976	0.193	0.433	5.59	5.0
total	0.5-10.0	1121	1.076	2.781	7.8	5.0
veryhard2	4.0-7.0	957	0.358	0.668	16.2	10.0
total2	0.5-7.0	1121	1.266	3.258	10.6	9.0


Fig. 3. Cumulative $\log N - \log S$ functions for X-ray sources detected in the SXDS field in the soft 0.5 - 2 keV (top) and total 0.5 - 10 keV (bottom) bands. Solid and dotted red lines show the data obtained in this work, presenting the full X-ray sample and the sample with optical counterparts, respectively. The dashed blue line presents the data obtained by Ueda et al. (2008) in the same bands.

described in Hodgkin et al. (2009). The AB limiting magnitudes at 2σ are 23.4, 23.4, and 22.9 in *J*, *H*, and *K* bands, respectively.

2.4. Mid-IR data

The SXDS field has been observed with the *Spitzer* telescope as part of the XMM-LSS field, one of the areas surveyed within the *Spitzer* Wide-area IR Extragalactic Legacy Survey (SWIRE). The public IRAC catalogue has been downloaded from the SWIRE web page¹⁰ and used in this work. It provides a set

of fluxes within five different aperture radii: 1.4, 1.9, 2.9, and 5.8 arcsec for the four IRAC channels (3.6, 4.5, 5.8, and 8.0 μm). Any source included in the catalogue, has been detected in both 3.6 μm and 4.5 μm bands. In order to convert the given fluxes to magnitudes we have used the following equation:

$$m[i] = 2.5 \log_{10}(F_{zero}^{[i]} / F_v^{quot}), \quad (1)$$

where $i = 3.6, 4.5, 5.8,$ and 8.0 are the four IRAC channels (Reach et al. 2005). F_v^{quot} is the flux density of a source from the calibrated images, and $F_{zero}^{[i]}$ are the zero-magnitude flux densities. The zero-magnitude fluxes have been determined by Reach et al. (2005) integrating the Kurucz model spectrum of αLyr over the IRAC pass-bands. The resulting zero-magnitude flux densities used in this work are 280.9 ± 4.1 , 179.7 ± 2.6 , 115.0 ± 1.7 , and 64.13 ± 0.94 Jy in the 3.6, 4.5, 5.8, and 8.0 μm channels, respectively. The total SWIRE XMM-LSS catalogue has $\sim 250,700$ objects. The AB limiting magnitudes at 2σ are 21.0, 21.1, 19.5, and 19.4 in 3.6, 4.5, 5.8, and 8.0 μm bands, respectively.

2.5. The catalogue of optical counterparts

Due to the very high number of detections in the optical bands (around 900,000 sources in both the *R_c* and *i'* bands, as noted in Section 2), there is a high probability of an erroneous identification when matching the X-ray and optical catalogues. In order to minimise such a risk, the optical catalogue has been first filtered. Based on previous results in the GWS field (Pović et al. 2009a), the optical flux has been constrained by assuming an upper limit of the X-ray-to-optical flux ratio¹¹, $X/O = 18$. We found this X/O ratio as a reasonable limit, since no sources have been found above this value in the GWS field. With this cut, and with the minimum X-ray flux of 8.9×10^{-16} erg cm $^{-2}$ s $^{-1}$ detected in the SXDS field, we obtained an upper limit in the optical range, and excluded all optical detections having AB magnitude $R_c > 27.17$. After applying this filter, the resulting catalogue is reduced from 901,094 *R* band sources to 614,857. This approach has proved to be consistent with the SXDS sample, since none of the X-ray sources with $F_{0.5-4.5\text{keV}} \leq 6.0 \times 10^{-15}$ erg cm $^{-2}$ s $^{-1}$ show $X/O > 18$, while only about 5% of the total number of sources exceed this limiting X/O value.

After filtering the optical catalogue, we followed the same cross-matching procedure as explained in Pović et al. (2009a). Comparing the number of unique counterparts and the number of multiple matches, the radii between 2'' and 3'' have been found to be the best compromise, selecting always as an optical

¹¹ Computed as $F_{0.5-4.5\text{keV}} / F_R$, where the optical flux F_R has been derived from the SExtractor auto magnitudes in the *R* band; See Section 4 for more information and references

¹⁰ http://swire.ipac.caltech.edu/swire/astronomers/data_access.html

counterpart a source closest to the X-ray detection. After applying the statistical methodology from de Ruiter (de Ruiter et al. 1977) a radius of $3''$ has been selected, obtaining a completeness of 99.9% and a reliability of 76.2%. The total number of optical counterparts obtained with this radius is 808. Additionally, for objects having multiple matches inside the selected radius, we performed the Sutherland & Saunders (1992) methodology measuring the reliability for all possible matches, and finally selecting as an optical counterpart an object with the highest probability. After this the number of possible fake identifications drops to $\sim 6\%$, where multiple matches are detected with similar probabilities. Regarding the ~ 300 X-ray sources not optically matched, 80 objects reside in the area not covered by optical observations; the rest of the objects might have been lost through optical catalogue filtering, they may be optically obscured sources, or some have resulted from fake X-ray detections (see Section 2.1).

2.6. Photometric redshifts and k -corrections

We used the Bayesian code ZEBRA (Feldmann et al. 2006) to compute photometric redshifts of the optical counterparts. Due to the small number of available spectroscopic redshifts used in the analysis (for only 15 sources obtained from Aretxaga et al. (2007), and references therein), as an additional check, photometric redshifts were also computed using the HiperZ code (Bolzonella et al. 2000). In both codes the templates from the SWIRE¹² template library were implemented and used, since they include the templates of AGN/QSO sources (Polletta et al. 2007). Comparing the results from ZEBRA and HyperZ, only those objects for which the redshift results from both codes agree within less than 0.1 for $z < 1$ and 0.2 for $z \geq 1$ were accepted. Finally, we derived high-quality photometric redshift information for 308 objects shown in Figure 4. The mean value of the final photometric redshifts is 1.17 ± 0.15 . Of those 86% of objects have photometric redshift errors below 20%.

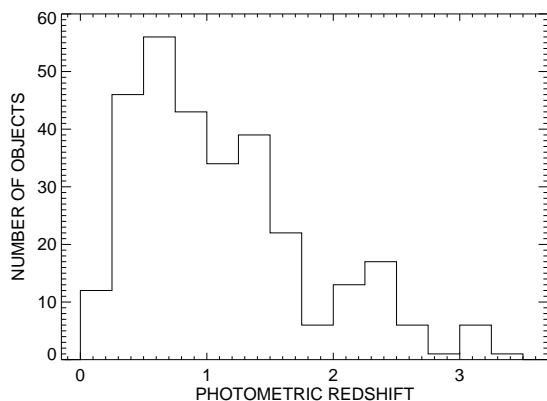


Fig. 4. Distribution of final photometric redshifts of X-ray emitters with optical counterparts.

In order to obtain k -corrections of the optical fluxes we have used the IDL routine KCORRECT (Blanton et al. 2007). The X-ray fluxes, on the other hand, were k -corrected by assuming a standard power law SED with $\Gamma = 1.8$. A rough classification between X-ray unobscured and obscured AGN has

been made using the hardness ratio $HR(2 - 4.5\text{keV}/0.5 - 2\text{keV})$ (see Section 4.3), which is quite sensitive to absorption (Della Ceca et al. 2004; Caccianiga et al. 2004; Dwelly et al. 2005); those objects with $HR(2 - 4.5\text{keV}/0.5 - 2\text{keV}) \leq 0.35$ (some 53%) have been considered as unobscured, and no intrinsic absorption has been applied to the power law SED; otherwise the objects have been considered as obscured and a fixed intrinsic absorption $N_{\text{H}} = 1.0 \times 10^{22} \text{ cm}^{-2}$ has been included (e.g., Silverman et al. 2005; Younes et al. 2011).

2.7. Selected sample

After performing de Ruiter et al. (1977) and Sutherland & Saunders (1992) methodologies when cross-matching X-ray and optical catalogues, and after considering only those objects with high-quality photometric redshift information, we remained with 308 sources in our sample. Of these, 262 sources (85%) have photometric redshifts $z \leq 2.0$. We obtained the morphological classification for all 308 objects (see Section 3), but we carried out all further analysis for a sample of objects with redshifts $z \leq 2.0$ and with redshift errors below 20%. For this sample we derived X-ray luminosities in all selected energy ranges. The average luminosity of $\log L_{\text{X}} = 43.7 \text{ erg s}^{-1}$ has been measured in the 0.5 - 7.0 keV band. Figure 5 shows the luminosity - redshift plane for X-ray detected AGN in the SXDS and GWS fields at $z \leq 2.0$.

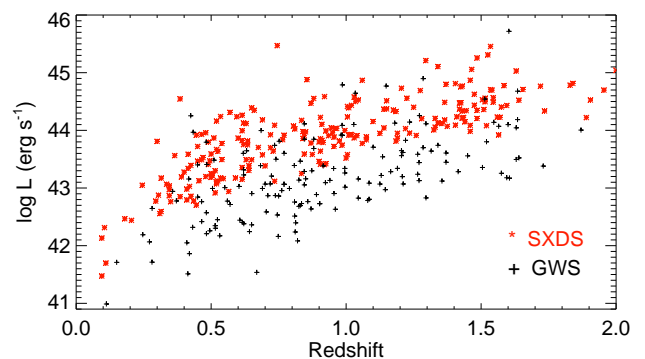


Fig. 5. Relation between the X-ray luminosity in the 0.5 - 7.0 keV band and redshift for a sample of AGN in the SXDS (red stars) and GWS (black crosses) fields.

The selected $z \leq 2.0$ sample presents around 25% of the initial X-ray sample, and 32% of the optically matched sample. In order to see if this sample is representative of the full X-ray population or of the matched one, we compared their X-ray flux distributions in all energy bands. Figure 1 shows these distributions in five energy bands for the parent X-ray sample and the analysed one. The selected sample seems to follow the distribution of full X-ray population in all observed bands quite well. Performing Kolmogorov-Smirnov statistics we obtained the probability parameter of 0.7 and 0.97¹³ in the 0.5 - 4.5 keV band (energy range used in AGN selection; see Section 4) when comparing the analysed sample with the full X-ray population and with the full optically matched sample, respectively.

¹³ Probability can take values from 0.0 to 1.0, where 1.0 means that the compared distributions are completely identical.

¹² http://www.iasf-milano.inaf.it/~polletta/templates/swire_templates.htm

Moreover, we compared X-ray and optical properties of the selected and full optically matched samples. Figure 6 (top) shows the relation between the X-ray flux in the 0.5 - 4.5 keV energy range and the AB R_c magnitude for these two samples. As again can be seen, the selected $z \leq 2.0$ sample covers the entire range of X-ray fluxes in comparison with the matched one. For a selected sample, there seems to be a shallow bias towards fainter sources in the optical range. However, when comparing the X-ray-to-optical flux ratios (Figure 6, down panel), the selected sample represents the full matched one quite well. For these two samples, the average $\log X/O$ ratios are 0.05 and -0.07, respectively.

To summarise, the $z \leq 2.0$ selected sample is a small fraction ($\sim 25\%$) of the full X-ray population (as mentioned above), but seems to follow the distributions of the initial X-ray and optically matched samples quite well.

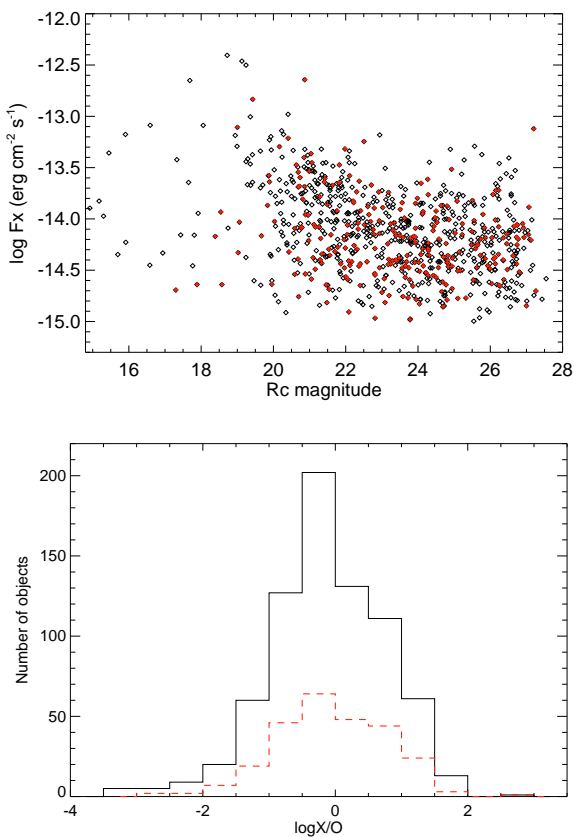


Fig. 6. *Top:* Relation between the X-ray flux in the 0.5 - 4.5 keV energy range and the AB R_c magnitude of the full matched sample (black diamonds) and of the selected sample (red crosses). *Bottom:* Distributions of X-ray-to-optical flux ratio of the full matched sample (black solid line) and of the selected sample (dashed red line).

Finally, in order to improve statistics, we included our data from the Groth-Westphal Strip (GWS) field when analysing the colour-magnitude relations. 174 objects were used, having photometric redshifts ≤ 2.0 and redshift errors below 20%. These data are deeper in X-rays in comparison with SXDS data, having X-ray limiting flux of 0.48×10^{-15} erg cm $^{-2}$ s $^{-1}$ in the 0.5 - 7.0 keV energy band. The detailed description of data, morphological and nuclear classifications can be found in Pović et al. (2009a). A small comparison between the luminosities in the

SXDS and GWS fields is also presented below (see Figure 5 and Section 2.6).

3. Morphological classification and analysis

3.1. Methodology

The morphology of the optical counterparts of X-ray emitters in the SXDS field was tested using SExtractor (Bertin & Arnouts 1996) and galSVM (Huertas-Company et al. 2008, 2009) codes. Moreover, as an additional check, a visual classification was performed as well.

First, compact objects were separated from extended ones. The SExtractor CLASS_STAR parameter was used to this end. This parameter permits the rough classification of objects as compact (QSOs, AGN with the weak host galaxies, stars, etc.) or extended. The computed value depends on the seeing, the peak intensity of the source and its isophotal area. The parameter ranges between 0 (for an extended object like a galaxy) and 1 (for a point-like object). A source has been deemed as compact if its CLASS_STAR parameter is ≥ 0.9 .

In order to separate between early- and late-type X-ray emitters (see Section 3.2 below), galSVM code has been used (Huertas-Company et al. 2008, 2009). galSVM¹⁴ is a freely available code written as an IDL library that, combined with the also freely available library libSVM¹⁵ enables a morphological classification of galaxies in an automated way using support vector machines (SVM¹⁶). This code represents a great improvement within non-parametric methods for morphological classification, being especially useful when dealing with low-resolution, and high-redshift data. It makes it possible to use a sample of objects with known morphology, to move these objects to the redshift and image quality of the sources that have to be classified, to test simultaneously different morphological parameters in order to find the best set for the morphological classification, and to use non-linear boundaries in order to determine the separation regions between different types. Different morphological parameters have been suggested and used in morphological classification over recent years (Abraham et al. 1996; Kent 1985; Bershady et al. 2000; Abraham et al. 2003; Conselice et al. 2003; Lotz et al. 2004), each of them providing different types of information about the structure of a galaxy. Before galSVM it was not possible to use more than 3 parameters simultaneously, forcing boundaries between different Hubble types to be linear (2D lines or hyper-planes). Therefore, besides being useful when dealing with high redshift and low resolution data, there are two main advantages of galSVM compared to other codes: first, it can use a list of morphological parameters simultaneously, and second, it can find and use non-linear boundaries in order to perform the final morphological classification. It has been shown that using galSVM to classify galaxies into two main morphological types (early- and late-type galaxies), provides a more reliable classification when compared to other non-parametric methods (Huertas-Company et al. 2008). Therefore, since we are dealing with low-resolution and

¹⁴ <http://gepicom04.obspm.fr/galSVM/Home.html>

¹⁵ Support Vector Machines library (libSVM), written by Chih-Chung Chang & Chih-Jen Lin, is an integrated program for support vector classifications, regressions, and distribution estimations; it supports the multi-parameter classifications.

¹⁶ Support Vector Machines (SVM) are a group of supervised learning methods that can be applied to classification or regression. Support Vector Machines represent an extension to non-linear models of the generalised portrait algorithm developed by Vladimir Vapnik (1995).

high-redshift data, we decided to use the galSVM code in order to separate between early- and late-type X-ray emitters in the SXDS field. galSVM requires the availability of redshift information for all examined objects. Therefore, morphology has been tested on the 308 X-ray sources with known photometric or spectroscopic redshifts. To perform the analysis, the i' optical band was chosen due to its higher S/N ratio.

We followed the complete and standard galSVM procedure, as described in Huertas-Company et al. (2008), in order to separate between early- and late-type X-ray emitters with optical counterparts:

1. We built a set of simulated galaxies, using a catalogue of local galaxies with known Hubble type (obtained by visual classification), redshift, total flux, and half luminosity radius. The Tasca & White (2011) catalogue was used for this purpose, containing 1504 visually classified local galaxies from the SDSS survey, observed in the g photometric band, which corresponds to the rest-frame¹⁷ band of the SXDS i' sample used with the average redshift of 0.8. Besides the local catalogue, subimages of all local galaxies and PSFs, necessary to run galSVM, have been gathered from Tasca & White (2011) as well. For each of the five SXDS fields observed in the optical i' band, we provided the magnitude and redshift distributions of our X-ray emitters with optical counterparts. Moreover, we run SExtractor on our real images in order to obtain the catalogue of all possible detections, as well as mask images. For every galaxy stamp used for training the morphology, galSVM generates a random pair of magnitude and redshift values with a probability distribution that matches that of our real data, in order to place the training galaxy in a real, high-redshift background image of our sources. Using the real images and SExtractor catalogues, the locations devoid of objects where the trained sample of galaxies could be placed are searched randomly, and then a SExtractor mask image is used to eliminate close objects.
2. After placing the sample of local galaxies in the high-redshift background of our real sample, we measured a set of morphological parameters of the training sample.
3. We trained a SVM with a fraction of 600 local galaxies and used the other fraction of 904 local galaxies to test the accuracy¹⁸, and to estimate errors. Then we repeated steps two and three to test different sets of morphological parameters and to choose the one that gives the most reliable morphological classification, which will be used afterwards for the classification of our real sample. As already mentioned, the galSVM accuracy parameter has been used as an indicator of classification reliability, but aside from the accuracy, the distributions of the obtained morphological parameters have been tested as well. It has been seen that there is a trend for bright objects to be identified as late-types with very high probabilities, increasing the value of the mean probability. Therefore, all brightness parameters (as mean surface brightness,

magnitude, flux) have been excluded from the initial set of parameters involved in the morphological classification. Table 2 shows the final set of parameters used to separate between early- and late-type galaxies. For this set of parameters an accuracy of 70% is obtained (see Section 3.2 below).

4. A set of morphological parameters has been obtained for all X-ray emitters with optical counterparts, and using the parameters from Table 2, morphological classification using galSVM was derived, correcting it for possible systematic errors detected in the testing steps.

3.2. Morphology of X-ray emitters

The morphological classification obtained, gives the result that early-type galaxies include elliptical and lenticular (although in some cases early-type spirals between S0 and Sa galaxies might be classified as early-type as well), while spiral and irregular galaxies have been classified as late-type. The output classification assigns to each galaxy a class label and a probability of belonging to a given class. When dealing with a 2-class problem (early- and late-type classification; see Huertas-Company et al. 2008), the probability p will be: $p_{\text{early-type}} = 1 - p_{\text{late-type}}$. Therefore, two probabilities are measured: $p_1 = p_{\text{early-type}}$ and $p_2 = p_{\text{late-type}}$, where for galaxy to be considered as early- or late-type the probability p_1 or p_2 must be higher than 0.5, respectively. The probability parameter is used to assess the accuracy of the morphological classification. There is a clear correlation between the probability threshold and the number of correct identifications: the accuracy clearly increases when the considered probability is higher. In Huertas-Company et al. (2009) it has been shown that selecting objects with a probability between 0.5 and 0.6 yields a mean accuracy of around 58%, while objects with probabilities greater than 0.8 are classified with nearly 90% accuracy.

As already mentioned in Section 3.1, the SExtractor STAR_CLASS parameter has been used to separate between compact and extended (host-dominated) objects. 22% of the total number of objects have been detected as compact, having a STAR_CLASS parameter ≥ 0.9 . Of those objects detected as early-type (with STAR_CLASS < 0.9 and $p_1 > 0.5$; 53% in total), 56% have probabilities ≥ 0.75 . Conversely, of objects identified as late-type (with STAR_CLASS < 0.9 and $p_2 > 0.5$; 18% in total) only 30% are found with probabilities $p_2 \geq 0.75$. A population of unclassified objects is 7% in total.

Several trends of the mean probability values have been tested (for both early- and late-types) with redshift, magnitude, and isophotal area (see Figure 7, upper panels). Since the trends of morphological parameters with distance, brightness, and size are also present in the training sample, the algorithm should be aware of such trends and should be able to take them into account in the final classification. For p_1 probabilities (early-type objects) there is only a weak trend with these parameters. Yet for p_2 probabilities (late-type objects) the trends seem to be more significant. This means that low p_2 probability objects (e.g., $p_2 < 0.7$) still have a big chance of being one of the late-types, but are detected with low probabilities since they are more distant, smaller, and/or fainter sources.

In order to check the obtained probabilities, a visual inspection of the images was also performed. It represents a traditional way of classifying galaxies between different morphological types, and it is rather subjective, but for bright and extended objects it can produce a high confidence level morphol-

¹⁷ As noted by Huertas-Company et al. (2008), selecting as the rest-frame band the training sample has three main advantages: (i) it is less affected by k-correction effects, (ii) it does not introduce any modelling effect, since the used galaxies are real, and (iii) it is possible to work with seeing limited data (as the training set is built to reproduce the observing conditions and physical properties of the sample to be analysed, but is classified using well-resolved images).

¹⁸ Accuracy represents the success rate in the morphological classification of the training sample; see Huertas-Company et al. (2008) for more information.

Table 2. Set of parameters used by galSVM for the final morphological classification of X-ray emitters in the SXDS field

ELONGATION ¹	CLASS_STAR
ABRAHAM CONCENTRATION INDEX ² ($\alpha = 0.3$)	ASYMMETRY ²
SMOOTHNESS ³	GINI COEFFICIENT ⁴
M ₂₀ MOMENT OF LIGHT ⁵	BERSHADY-CONSELICE CONCENTRATION INDEX ⁶

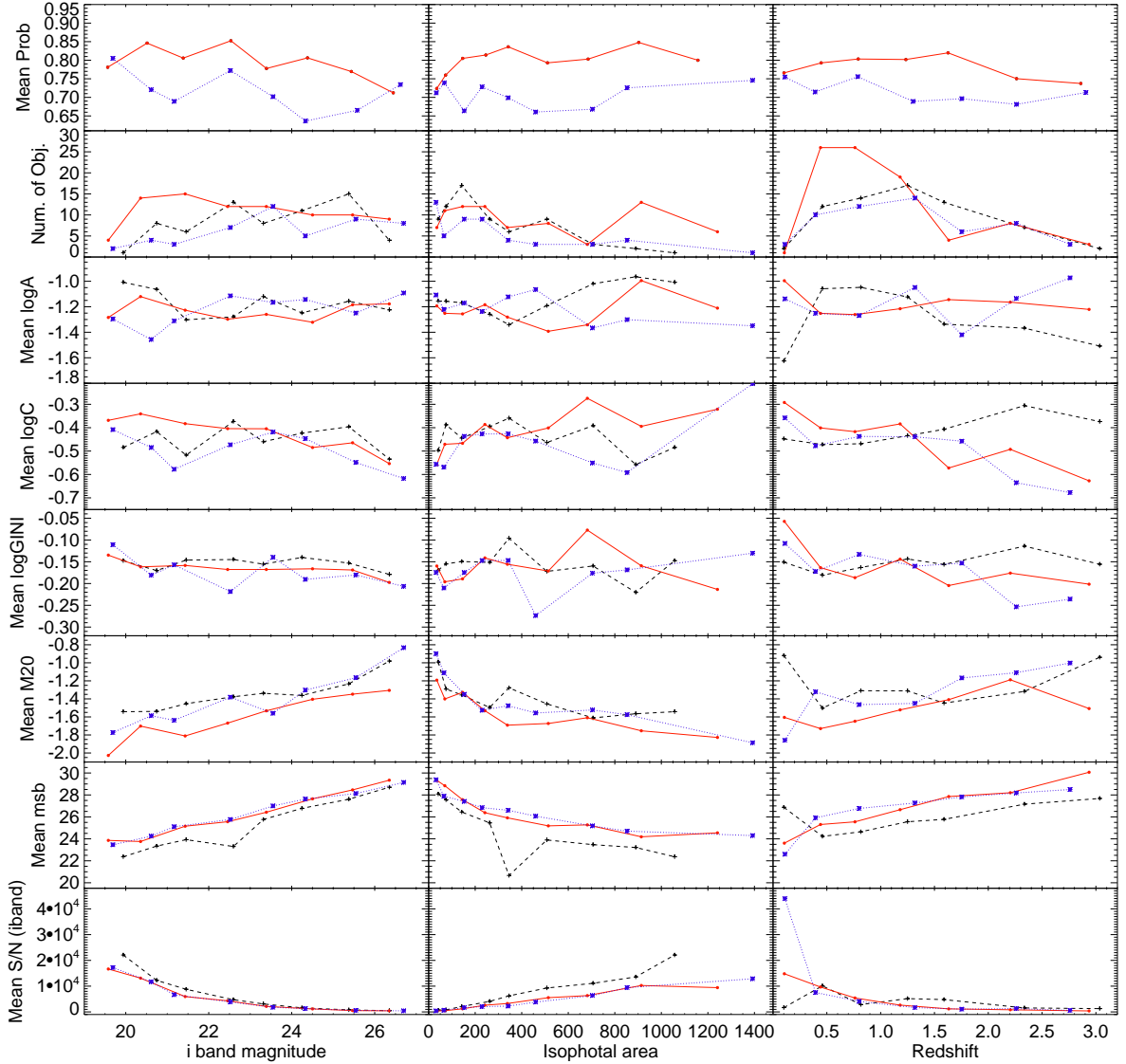
¹ Ratio between the major and minor axes (A_IMAGE and B_IMAGE SExtractor parameters; Bertin & Arnouts 1996)

² Abraham et al. (1996)

³ Conselice et al. (2003)

⁴ Abraham et al. (2003)

⁵ Lotz et al. (2004)

⁶ Bershady et al. (2000)

Fig. 7. From top to bottom: Relationship between mean values of galSVM probabilities, number of objects, asymmetry index, Abraham concentration index, Gini coefficient, M₂₀ moment of light, mean surface brightness, S/N in i band, and (from left to right:) apparent magnitude in i' band, isophotal area, and redshift. Compact objects are marked with black crosses and dotted lines, early-type galaxies with red spots and solid lines, and finally, late-type galaxies with blue stars and dashed lines.

ogy, and may be a helpful tool to probe the reliability of different structural parameters computed with automated meth-

ods. To this end, the IRAF/*imexam* tool has been used in order to obtain the isophotal contour diagrams, providing infor-

mation of bulge/disc dominated objects (for more information see Pović et al. 2009a). For objects classified as compact and late-type there is a good correspondence between automated and visual classification. Conversely, for objects classified with galSVM as early-type galaxies, having p_1 probabilities ≥ 0.75 there is a good correlation with visual inspection, while in cases of lower p_1 probabilities ($0.5 < p_1 < 0.75$), the number of possible interactions starts to grow, as well as the number of objects with low S/N ratio, being possible late-type objects. Therefore, in the further analysis only high-probability ($p_1 \geq 0.75$), early-type objects have been considered in the early-type class.

Figure 8a shows a standard morphological classification diagram, comparing the asymmetry parameter (A) and Abraham concentration index (C). This Figure has been used roughly to separate the areas where most of early- (only objects with $p_1 \geq 0.75$; red dots) and late-type galaxies (all objects with $p_2 > 0.5$; blue stars) are located. The separation is shifted with respect to that defined by Abraham et al. (1996; see their Figure 5). This could be expected at for least two reasons: first, a number of early-type spirals (between S0 and Sa galaxies) enter in the early-type classification obtained by galSVM, and/or second, different methods have been used in order to obtain concentration and asymmetry indexes. Moreover, as already mentioned, in this work the morphological classification was not solely based on this two-parameter diagram, but rather on 8 parameters that have been used by galSVM (see Table 2). As discussed in more detail in Section 3.3, it seems that a multi-parameter space with non-linear separations is necessary in order to separate early- from late-type galaxies accurately. This is one of the main galSVM advantages in comparison to other morphological classification codes. In the same Figure we also show objects having early-type class probabilities $0.5 < p_1 < 0.75$ (open diamonds). These objects cover both areas, with a possibility of being either early-, late-type galaxies or interacting systems, as explained above.

3.3. Difficulties in morphological classification

- **Systematic trend with brightness, size, and redshift.** The relations between the different morphological parameters and apparent magnitude (in the i' band), size (isophotal area), and distance (redshift) have been tested for a sample of SXDS X-ray emitters analysed in this paper, belonging to different morphological types: compact, early- ($p_1 \geq 0.75$), and late-type objects ($p_2 > 0.5$). Figure 7 shows the mentioned relations for the asymmetry and Abraham concentration indexes, Gini coefficient, M_{20} moment of light, and mean surface brightness. The mean number of objects and S/N ratio in i' band are represented as well. There is a certain trend of observed morphological parameters with the apparent magnitude, size, and distance. Parameters related with the galaxy concentration (C, Gini, and M_{20}) seem to be more affected than the asymmetry index. In other words, fainter, smaller and more distant objects show systematically lower light concentrations. This can be due to detection effects, but aside from this, it might also be related to the intrinsic properties of the galaxies: fainter and/or smaller objects are intrinsically less concentrated (e.g., Blanton et al. 2001). In general, the parameters of the objects detected as compact seem to be less affected with brightness, size, and redshift than early- or late-types. On the other hand, early- and late-type galaxies seem to show similar trends. However, as already mentioned above, the code is taking these trends into account in the final classification since the same ones are also present in the local training sample.

- **Low S/N ratios.** The bottom panels in Figure 7 show how the S/N ratio in i' band changes with brightness, size, and distance. As already mentioned in the previous two sections, a low signal-to-noise ratio increases the uncertainty in the morphological classification. Two effects can therefore be observed:

- As the S/N decreases, the information from the galactic disc can be lost. This results in the possibility that a group of late-type galaxies can be classified as early-type, while early-type galaxies may be detected as compact. Low S/N ratio affects all morphological parameters, those related with the asymmetry/smoothness, as well as those related with the galaxy light concentration.
- Low S/N ratios can affect the bulge information as well. For example, it can be observed how the Abraham concentration index changes as the S/N decreases in a bulge-dominated or compact object. It can be expected that a low S/N ratio will smooth out the galaxy profile affecting regions far away from the centre more severely. Thus the galactic radius (used to calculate the concentration index as the ratio between the total flux and the flux at 30% of the radius) will decrease as well. Both F_{tot} and F_{30} fluxes will be affected, but larger impact will correspond to F_{30} , which could decrease significantly, leading to lower values of the galaxy light concentration. Therefore, bulge-dominated objects with low S/N ratios will have lower concentrations (than the ones with high S/N), placing them in the regions populated by late-type objects. Nevertheless, most of these diagrams can be used to define the region where most of the compact objects are located, as shown in Figure 8.

- **Number of parameters needed for the morphological classification.** As already stated, various structural parameters have been obtained with galSVM in order to characterise the morphology of the X-ray emitters in the SXDS field. The relationship between them has been studied after obtaining the final morphological classification. It has been seen that for the observed sample of objects the combination of any two parameters is not enough to separate between early- and late- type galaxies. The classification in a multi-parameter space with non-linear separations is needed, as done with galSVM. However, besides the $\log A$ vs. $\log C$ diagram (see Abraham et al. 1996), represented in Figure 8a, the smoothness and M_{20} moment of light parameters related with the Abraham concentration index, and the mean surface brightness related with the M_{20} moment of light make it possible to define the best probability regions of finding compact, early- and late-type objects, as shown in Figures 8b, c, and d, respectively, although the dispersion between the classes is still significant. A linear correlation has also been seen between the four parameters related with galaxy concentration (Abraham and Bershady-Conselice concentration indexes, Gini coefficient and M_{20} moment of light), as well as between the mean surface brightness and C and Gini (see Figure 8e, f). However, aside from the M_{20} -C diagram, for the observed sample they do not provide a good method for separating early- and late-type morphologies.

3.4. Morphological classification: summary

The catalogue that provides the final morphological classification and the list of morphological parameters and other data obtained in this work, is described in Appendix A, and is available in the electronic edition of this paper.

Having performed a morphological study of X-ray emitters

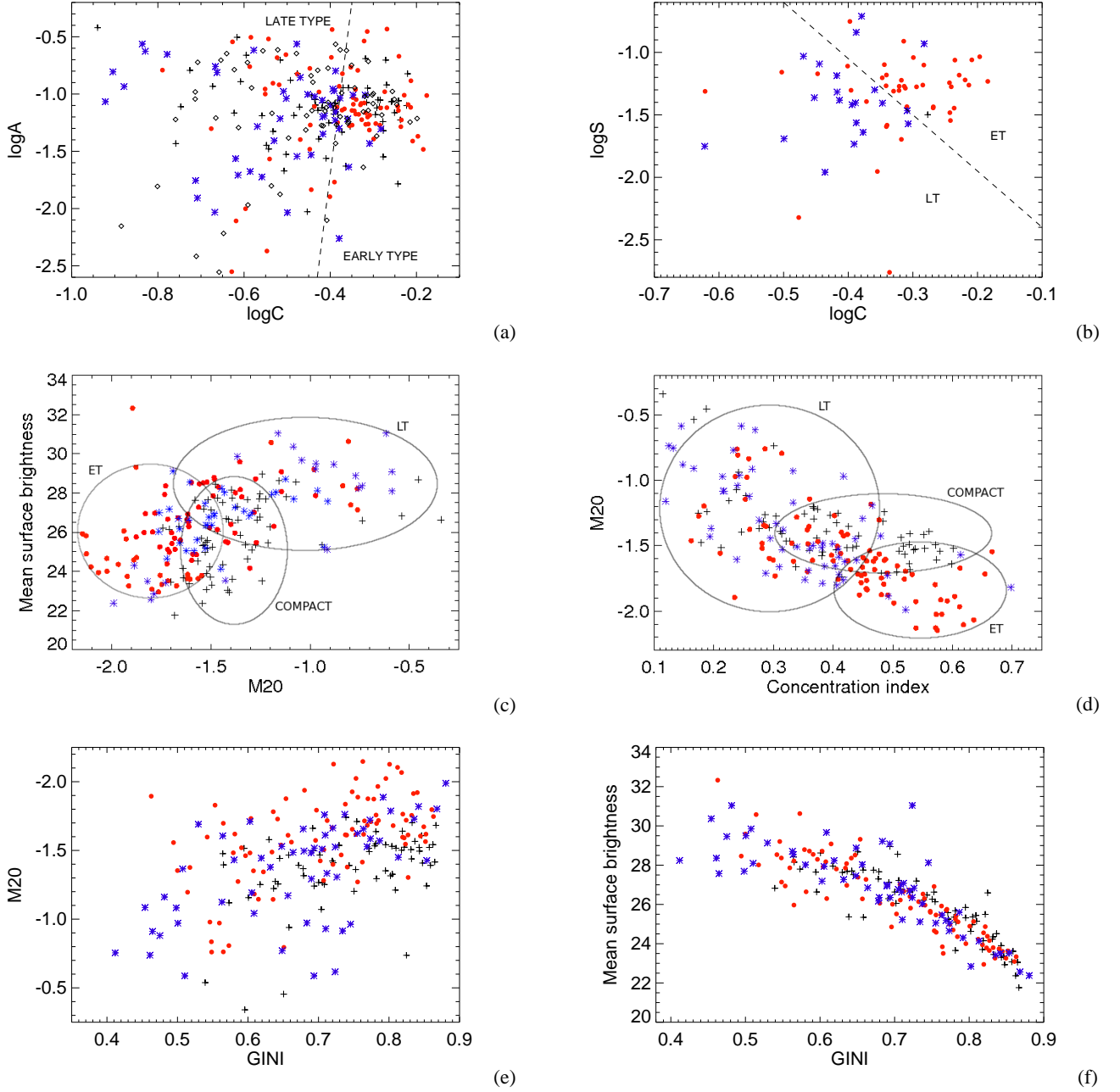


Fig. 8. *Top left:* Relation between asymmetry and Abraham concentration index. Red dots represent the early-type galaxies (E/S0, S0/Sa) classified with probabilities $p_1 \geq 0.75$, while the blue stars represent all late-type galaxies having p_2 probabilities above 0.5. Black crosses represent compact objects (all sources with $\text{CLASS_STAR} \geq 0.9$). Open diamonds are sources with $0.5 < p_1 < 0.75$, which might be either ET/LT or mergers (see Section 3.2). The dashed line separates the areas where most of the early- and late-type galaxies are located (right and left area from the dashed line, respectively). *Top right:* Relation between the smoothness and Abraham concentration index. The dashed line separates the areas where most of the early- (on the right; red dots) and late-type (on the left; blue stars) galaxies are located. Relation between the mean surface brightness and M_{20} moment of light (*Middle left*), and between the M_{20} moment of light and Abraham concentration index (*Middle right*). Symbols are the same as on the previous two plots. High probability regions of finding any of three morphological groups (early-, late-, or compact sources) have been defined in both plots. *Bottom left:* Relation between the M_{20} moment of light and Gini coefficient. See previous plots for symbols description. *Bottom right:* Relation between the mean surface brightness and Gini coefficient. See previous plots for symbols description.

with optical counterparts in the SXDS field, it can be concluded that the sources analysed in this paper are predominantly hosted by luminous spheroids and/or bulge-dominated galaxies. At least 55% of the hosts are compact or E/S0/S0-Sa galaxies. Table 3 summarises the final morphological classification of the selected

sample, a subsample of the full X-ray population. Although the selected sample seems to be representative of the full X-ray population (see Section 2.6), the results presented here should not exclude the possibility that the remaining 73% for which mor-

phological classification was not possible may be dominated by later types.

Table 3. Summary table: Morphology of X-ray emitters with optical counterparts in the SXDS field

Morphology	Comment
22% compact	
30% early-type	$p_1 \geq 0.75$
23% early-/late-type or possible interactions	$0.5 < p_1 < 0.75$
18% late-type	$p_2 > 0.5$
7% unidentified	

As will be commented in Section 4.3, most (if not all) of the X-ray emitters analysed in this paper are AGN. Therefore, the results obtained in this work can be compared with previous results on host galaxy morphologies of X-ray selected AGN.

In general, the morphological classification performed in this work confirms some of the latest findings that indicate that most X-ray detected AGN are hosted by spheroids and/or bulge-dominated galaxies (e.g., Grogin et al. 2005; Pierce et al. 2007; Gabor et al. 2009; Pović et al. 2009a; Georgakakis et al. 2009; Griffith & Stern 2010). Pierce et al. (2007) used a sample of 94 intermediate-redshift AGN ($0.2 \leq z < 1.2$), selected using *Chandra* X-ray data and *Spitzer* MIR data in the Extended Groth Strip (EGS) field. Basing their classification on M_{20} moment of light and Gini coefficient, they found that X-ray selected AGN mostly reside in bulge-dominated galaxies ($53^{+11}_{-10}\%$), which is in good agreement with our study taking into account both galaxies classified as compact and early-type. Our results are also in good agreement with Georgakakis et al. (2009) who used the high resolution optical data from the Hubble Space Telescope (HST) to study the morphological properties of a large sample of X-ray detected AGN. They found that a majority of their objects are bulge-dominated galaxies. Compared with the latest analysis performed by Griffith & Stern (2010) we found a lower number of compact sources, but a higher number of early-type bulge-dominated galaxies.

Most of the objects morphologically classified have redshifts $z < 2.0$ (although a small fraction of 16% have photometric redshifts $z > 2.0$), which indicates that nuclear activity remains preferentially associated with bulge-dominated galaxies out to substantial look-back times. Figure 9 shows the normalised distribution of different morphological types with redshift, suggesting that the objects from our sample classified as early-type reach a peak around $z \sim 0.8$, while the maximum distribution of late-type objects peaks at higher redshifts, $z \sim 1.2$. Most of the objects detected as compact have been found around $z \sim 1.0$.

As shown in Georgakakis et al. (2009) and references therein, studying the morphology of the AGN host galaxies can be an important way of addressing the issue of the AGN fuelling mechanisms, by placing robust limits on the relative contribution of the different mechanisms (e.g., major mergers, minor interactions, internal instabilities) to the accretion history. In the standard view of hierarchical structure formation, spheroidal and early-type bulge-dominated galaxies suffered major mergers in their past that destroyed any pre-existing discs to form a bulge dominated remnant (e.g., Barnes & Hernquist 1996; Springel & Hernquist 2005; Hopkins & Hernquist 2009). Hence we can conclude that different mechanisms may be responsible for putting a galaxy in an active phase. As shown above, at least

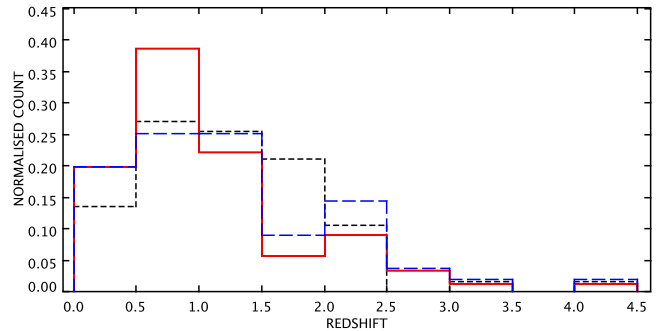


Fig. 9. Normalised redshift distributions of compact (short-dashed black line), early- (solid red line), and late-type (long-dashed blue line) sources.

50% of X-ray detected AGN analysed in this work reside in spheroids and/or bulge-dominated systems, suggesting that they might have undergone major mergers in their accretion history. However, at least 18% of the AGN seem to have disc galaxy hosts, showing therefore that minor interactions, internal instabilities, and/or some other secular mechanisms could also play an important role in accretion and black hole feeding.

4. AGN colour-magnitude relations (CMRs)

As already mentioned, besides morphology, colours are essential for studying the properties of AGN host galaxies and their connection with the AGN phenomena. Using a large sample of X-ray selected AGN, we have analysed colour-magnitude diagrams in order to study their relationship with other properties of active galaxies. The sample used in this study has two main advantages, when compared to those used in previous works: on the one hand, it is much larger, and on the other, it represents one of the deepest optical datasets to date.

To measure the colours of AGN, only objects having $\log X/O \geq -1$ have been examined, the typical values for active galaxies, where X-ray fluxes are measured in the 0.5-4.5 keV energy range and optical in the R band (e.g., Fiore et al. 2003; Della Ceca et al. 2004). Besides the AGN sample selected in the SXDS field, a sample of AGN selected in the GWS field has also been used (Pović et al. 2009a). This extended sample has been compared with a population of normal galaxies belonging to the CDF-S field (Wolf et al. 2001, 2004, 2008). SXDS optical data are deeper than CDF-S data (and deeper than most (if not all) other ground based photometry optical surveys), however only 20% of active galaxies from our sample have magnitudes above the completeness limit of CDF-S data. Nonetheless, this survey has the information necessary for our comparisons publicly available for a large sample of normal galaxies. The CDF-S catalogue contains 50,000 objects; from these, those objects classified by the COMBO-17¹⁹ survey as ‘Galaxy’ (44,925 sources) have been used in this work as a comparison sample. Following Wolf et al. (2001, 2004, 2008), the selected sample could contain up to a few dozen Seyfert-1 objects, as well as few dozens Seyfert-2 galaxies. However, compared with the population of normal galaxies, just a small contribution of

¹⁹ Classifying Objects by Medium-Band Observations - a spectrophotometric 17-filter survey; http://www.mpia.de/COMBO/combo_index.html

these objects is expected to be found (Wolf et al. 2001, 2004, 2008). Therefore, we do not expect that such a small fraction of these active galaxies can contaminate significantly the sample of non-active galaxies selected and used in this work, thereby changing the derived conclusions. Moreover, considering that the sample of normal galaxies has been classified by the COMBO-17 survey using all the available spectrophotometric information in 17 filters, it should be good when comparing the colours between normal and active galaxies, without introducing a possible selection bias.

As noted in Section 2.6, in all colour-magnitude diagrams, we only analysed objects with photometric redshifts $z \leq 2$ and with errors below 20%, in order to avoid the possibly less reliable measurements. There are 262 objects in total fulfilling these conditions.

4.1. CMRs in relationship with redshift

Figure 10 shows the CMR between the rest-frame $B - V$ colour and the absolute magnitude in the B band (M_B) for the population of AGN in the SXDS and GWS fields, and for a comparison sample of normal galaxies from the CDF-S field. Moreover, this CMR has been analysed in four redshift intervals: $z \leq 0.5$, $0.5 < z \leq 1.0$, $1.0 < z \leq 1.5$, and $1.5 < z \leq 2.0$, as shown in Figure 11. Rest-frame colours of normal galaxies have been obtained from the CDF-S catalogue (Wolf et al. 2001, 2004, 2008), while for the sample of AGN the rest-frame colours and the absolute magnitudes have been computed from the k-corrected apparent magnitudes. The population of normal galaxies shows the already mentioned bi-modality of colours at all observed redshifts. We plotted on all diagrams the Melbourne et al. (2007) rest-frame colour separation ($B - V = 0.6$), in order to distinguish between galaxies belonging to the red sequence (those with $B - V > 0.6$) and the blue cloud (those with $B - V < 0.6$).

As shown in Figures 10 and 11, we can confirm some of results found in previous works (e.g., Nandra et al. 2007; Georgakakis et al. 2008; Silverman et al. 2008; Schawinski et al. 2009): most X-ray selected AGN reside in the green valley (the region between the red sequence and blue cloud), at the bottom of the red sequence, and at the top of the blue cloud. At least $\approx 60\%$ of the AGN in the SXDS and GWS fields are located in this region of the colour-magnitude diagram, having absolute M_B magnitudes in the range $-18.0 \leq M_B \leq -21.5$, and rest-frame colours in the range $0.3 \leq B - V \leq 0.9$. If we compare the distributions of rest-frame $B - V$ colours for red and blue AGN and for normal galaxies, it can be seen that the distribution of red AGN peaks towards bluer colours ($B - V \approx 0.62$) while the distribution of blue AGN peaks toward redder colours ($B - V \approx 0.57$), in comparison with the sample of red and blue normal galaxies ($B - V \approx 0.7$ and ≈ 0.3 , respectively). As shown in Figure 11, AGN start to populate the green valley at higher redshifts, $z > 0.5$. Analysing the number of sources in redshift bins with a width of 0.1, the maximum number of AGN has been found at $z \approx 0.9$.

Besides the green valley where most AGN reside, a number of very luminous ($M_B \lesssim -21.5$), blue sources (rest-frame $B - V \leq 0.2$) lie outside the region covered by the normal galaxy population (Figure 10). They are all very luminous X-ray sources, having luminosities $L_X \geq 10^{44} \text{ erg s}^{-1}$ in the 0.5 - 7.0 keV energy range. Moreover, practically all of these sources have been classified as compact (see Section 4.2 for more details). This region corresponds to QSO objects. Around 10% of the total sample of the AGN studied in this work

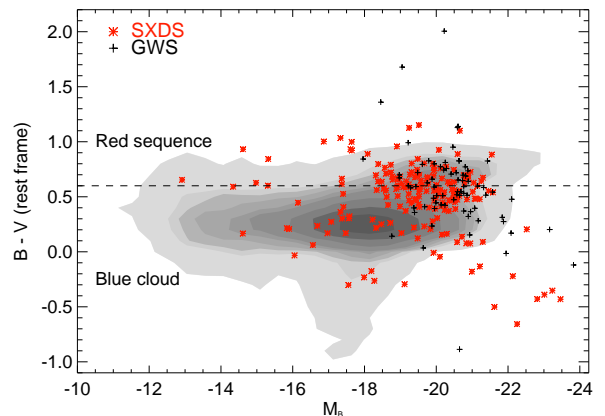


Fig. 10. Colour-magnitude diagram showing the relationship between the rest-frame $B - V$ colour and the absolute magnitude in the B band for a sample of AGN in the SXDS (red stars) and GWS (black crosses) fields having redshifts $z \leq 2$. The sample of AGN is compared with a sample of normal galaxies from the CDF-S field (Wolf et al. 2001, 2004, 2008) represented by contours. The gray scales of the contours are scaled to the data, where the darkest and brightest show the highest and the lowest density of the sources, respectively. The dashed line shows the Melbourne et al. (2007) separation between the red sequence ($B - V > 0.6$) and blue cloud ($B - V < 0.6$) galaxies. Median error bars are 0.0083, and 0.0325 for the absolute magnitude in the B band, and 0.0198, and 0.0489 for the $B - V$ rest-frame colour, in the SXDS and GWS fields, respectively.

reside in this area. They start to populate the colour-magnitude diagrams at higher redshifts ($z > 1$), as shown in Figure 11.

In comparison with previous works, we detected a much larger population of low-luminosity AGN ($M_B \gtrsim -18.0$), most of them at redshifts < 1.0 , being located in both the blue cloud and red sequence. Around 15% of AGN from the whole sample have been found to lie in this region. These AGN can occupy a wide range of rest-frame colours ($-0.4 \leq B - V \leq 1.1$), with most of them having X-ray luminosities above $10^{43} \text{ erg s}^{-1}$ in the 0.5 - 7.0 keV energy range. All these objects belong to the SXDS field and have been detected for the first time thanks to the large depth of the optical data.

As already shown, it seems that the colours of X-ray detected active galaxies differ from those of non-active galaxies, in all observed redshift intervals. Normal galaxies show clear bi-modality at all redshifts, belonging to the red sequence or blue cloud, while no colour bi-modality has been found for AGN. Usually galaxies residing in the green valley are considered to be transition sources, transiting from blue, star-forming galaxies to red, passively-evolving early-type objects. Therefore, since most AGN have been found in this region, it has been suggested in several previous works that there is a relationship between the mentioned transition and the AGN activity, and that AGN feedback might be responsible for quenching the star formation in blue cloud galaxies, moving them to earlier types (e.g., Nandra et al. 2007; Georgakakis et al. 2008; Silverman et al. 2008; Treister et al. 2009; Springel et al. 2005; Schawinski et al. 2006; Hasinger 2008).

However, there are a few aspects that should be considered

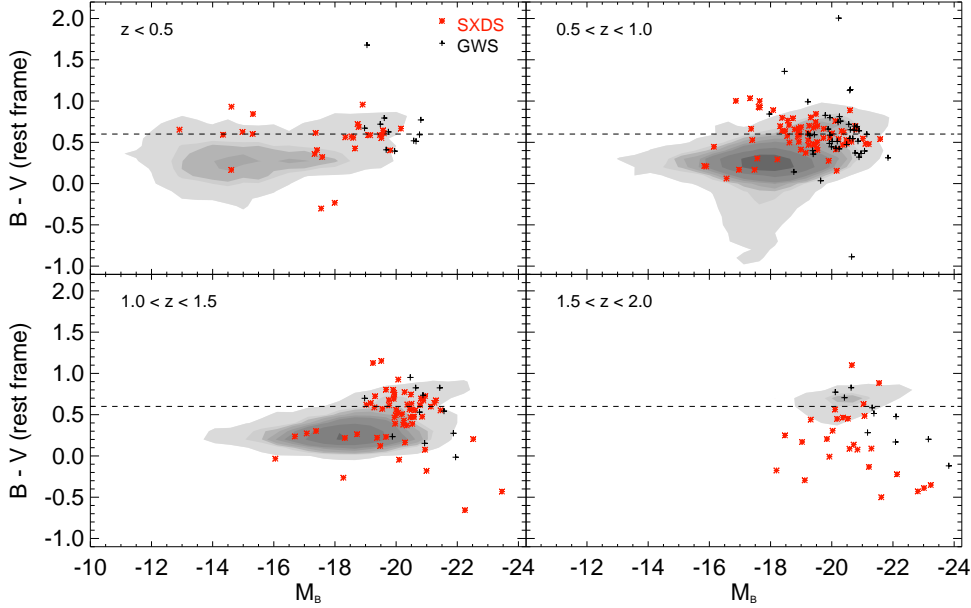


Fig. 11. The same colour-magnitude diagram as shown in Figure 10, but presented in four redshift intervals, from up to down, and from left to right: $z \leq 0.5$, $0.5 < z \leq 1.0$, $1.0 < z \leq 1.5$, and $1.5 < z \leq 2.0$.

when comparing colours of normal and active galaxies:

- **Completeness limit of the comparison galaxies.** We checked the completeness limits of both the AGN and control samples, finding that $\sim 20\%$ of AGN ($\approx 22\%$ and $\approx 17\%$ in the B band and V band, respectively) have magnitudes above the completeness limit of the comparison non-active galaxies, which is insufficient population for changing the general picture of AGN distribution in the colour-magnitude diagrams.

- **AGN contribution.** The AGN contribution to the host galaxy emission has not been quantified in this work. It has been analysed by other authors, suggesting that the galaxies hosting AGN with low X-ray luminosities ($\log L_X \lesssim 44$), being mostly located in the green valley, should be moved to even redder colours after the AGN contribution is eliminated and the total galaxy flux corrected (Kauffmann et al. 2007; Nandra et al. 2007; Silverman et al. 2008). Recently, using HST images, Cardamone et al. (2010) studied how the light from the central nuclear source affects the colours of moderate luminosity AGN host galaxies in the GOODS survey. They found that the integrated optical galaxy light is dominated by host emission, and that optical colours are not significantly affected by AGN emission. Moreover, Pierce et al. (2010) found that only in some $< 10\%$ (when the AGN is very luminous, unobscured, and/or compact) X-ray selected AGN can affect significantly integrated optical and UV colours; otherwise, the AGN contribution to the integrated optical/UV colours is not significant.

- **Dust reddening.** In several previous works, it has been found that many blue, star-forming galaxies being reddened by dust have colours that would place them in the green valley. This could mean that many green valley galaxies are not transition sources, evolving from blue to passively-evolving red galaxies, but rather blue cloud sources being affected by dust. Moreover, a possible selection effect could be introduced, observing AGN less affected by extinction, since the most reddened AGN might

have magnitudes below the detection limits. Using NIR colours to separate between the red early-type galaxies and galaxies being reddened by dust (at $0.8 \leq z \leq 1.2$), Cardamone et al. (2010) found that $\sim 25\%$ and $\sim 75\%$ of AGN belonging to the red sequence and green valley, respectively, actually have colours typical of young stellar populations being reddened by dust, and that their dust-corrected optical colours are blue and similar to those of star-forming galaxies. However, using dust-corrected optical colours, Xue et al. (2010) found a very weak colour bi-modality for AGN host galaxies at redshifts $z \leq 1.0$, and no evidence at higher redshifts, suggesting that even after dust-correction active galaxies still appear redder than non-active galaxies, at all redshifts. We have studied the effect of dust-reddening in our sample of late-type AGN selected in the SXDS field. In order to obtain the extinction in both B and V bands, and the extinction corrected rest-frame $B - V$ colour, we used the same corrections as in Fernández Lorenzo et al. (2010). As noted in that paper, using the Tully et al. (1998) method the extinction A_B in the B band can be measured as a function of the inclination i , through major-to-minor axis ratio a/b : $A_B = \gamma_B \log(a/b)$, with $\gamma_B = -0.35 (15.31 + M_B)$. These formulae have been derived using a sample of spiral galaxies and the Vega magnitudes. Therefore, we are dealing with Vega magnitudes when analysing the extinction correction, studying only galaxies classified as late-types. The major and minor axes have been obtained by SExtractor. As noted by Fernández Lorenzo et al. (2010), using Calzetti et al. (2000) the extinction in the V band can be calculated as $A_V = 0.8 A_B$. Figure 12 (left panel) shows the relationship between the inclination and the obtained extinction in the B band. After applying the extinction corrections, we did not find any significant difference in the colour distribution of late-type AGN. Figure 12 (right panel) shows the comparison for the $B - V$ colour before and after applying the extinction correction. Moreover, applying the Kolmogorov-Smirnov analysis, we

obtained a significance level of 0.72, showing that the cumulative distribution function of $B - V$ colour is not significantly different before and after applying the extinction correction. This would mean that even after the extinction correction, the late-type galaxies, which should be more affected by dust reddening as compared to early-types, will mostly stay placed in the green valley. However, the extinction correction applied here is only a coarse one, since the used equations have been derived for the local universe, and no corrections related with the possible evolution of dust content with the redshift have been applied.

Conversely, other results show that when comparing samples of active and normal galaxies with similar stellar masses and being at similar redshifts, AGN host galaxies do not show a strong evidence for either quenched or elevated star formation (e.g., Alonso-Herrero et al. 2008). Moreover, studying the CMRs of X-ray selected active and non-active galaxies at high redshifts $z \approx 1 - 4$, Xue et al. (2010) found a colour bi-modality in non-active galaxies that is absent in AGN hosts. This holds up to $z \approx 3$ (in good agreement with the results mentioned above). Yet using stellar mass-selected samples they found that the difference in the colour distribution between active and non-active galaxies disappears, and that mass-selected AGN hosts have the same bi-modal distribution in the CMRs as non-active galaxies, up to $z \approx 2 - 3$. The authors suggested that AGN preferentially reside in massive galaxies that normally tend to have redder colours. However, these results are in contrast with the ones obtained by Schawinski et al. (2010) in the nearby universe, where the colours of mass-selected AGN still peak in the green valley.

We measured the stellar masses of our active galaxies (from both the SXDS and Groth fields) and of the control sample using the same procedure explained in Xue et al. (2010). Figure 13 shows the relation between the stellar mass in B band and rest-frame $B - V$ colour. For a sample of AGN studied in this work, even when mass-matched with a sample of inactive galaxies, we do not find a clear colour bi-modality. Around 60% of AGN from our sample reside between the red sequence and blue cloud, having stellar masses between $10^{9.7}$ and $10^{11} M_{\odot}$. This is a similar population to that found residing in the green valley of colour-magnitude diagrams (see Figure 10). However, in comparison with Xue et al. (2010), we are dealing with different stellar mass populations, that have a lower fraction of galaxies at redshifts between 1.0 and 2.0, and without a population of the most massive galaxies (above $10^{11} M_{\odot}$) they found residing in the red sequence.

4.2. CMRs in relationship with morphology

As mentioned above, CMRs have been used in previous studies as a tool to analyse the role of AGN activity and AGN feedback in galaxy evolution (e.g., Nandra et al. 2007; Georgakakis et al. 2008; Silverman et al. 2008; Schawinski et al. 2009). In previous works this type of analysis has usually been performed using a whole population of AGN. In order to understand the role of AGN in galaxy evolution, it is necessary to study the colour-magnitude diagrams for different morphological types (instead of the whole population), at both low and high redshifts. This is one of the first works where CMRs are studied in relationship with morphology using a high-redshift (up to $z = 2$) magnitude limited AGN sample.

Figure 14 shows the CMRs of X-ray selected AGN in the SXDS and GWS fields, taking into account the morphological classification of sources. Colour-magnitude diagrams are presented for compact sources, and for two main morphological

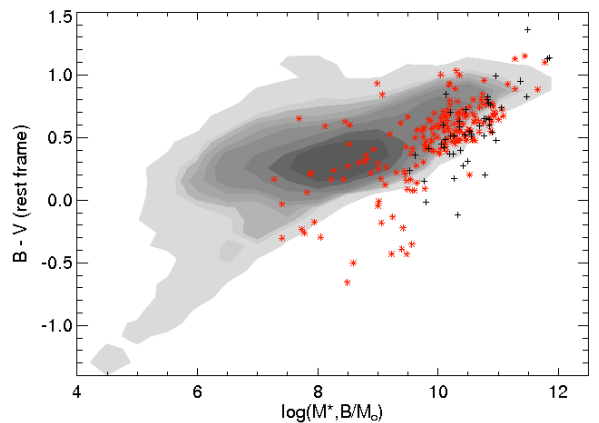


Fig. 13. Relation between the rest-frame $B - V$ colour and the stellar mass in the B band for a sample of AGN in the SXDS (red stars) and GWS (black crosses) fields having redshifts $z \leq 2$. See Figure 10 for a description of a control CDFS sample represented with grey contours.

types, early- and late-type AGN host galaxies. All AGN with redshifts $z \leq 2.0$ are shown. The morphological classification of active galaxies belonging to the SXDS field has been described in Section 3. For the selection and morphological classification of AGN in the GWS field see Pović et al. (2009a). Groups classified as I and II in Pović et al. (2009a) have been presented here as early-, and groups III and IV as late-type galaxies. As in Figures 10 and 11, for each morphological type the distribution of active galaxies has been compared with the distribution of the global population of normal galaxies from the CDF-S field.

As can be seen in Figure 14, $> 85\%$ of sources classified as compact have blue colours, with many of them residing in the green valley. A significant number of these sources are QSOs, but AGN with faint hosts, and spheroidal galaxies are also presented. Around 25% of the compact sources reside in the region devoid of normal galaxies, with very blue colours and high luminosities typical of high redshift QSOs.

On the other hand, no clear separation has been found between early- and late-type galaxy hosts on the colour-magnitude diagrams. Both types seem to follow a similar distribution, being again mostly located in the green valley, at the bottom of the red sequence, and at the top of the blue cloud. Therefore, a sample of AGN analysed in this work does not show a clear relationship between the colours and morphology. On the other side, colours of active galaxies can be influenced by AGN and/or dust obscuration, moving the early-/late-type sources toward the blue cloud/red sequence, respectively. However, as already noted in Section 4.1, we still need more work in order to quantify these contributions.

As already mentioned above, this is one of the first works in which AGN colour-magnitude relations have been studied according to morphology, for AGN at $z \leq 2$. Only recently, Schawinski et al. (2010) studied colour-stellar mass diagrams (instead of colour-magnitude relations) but in the nearby universe ($z < 0.05$) for early- and late-type AGN host galaxies. On these diagrams they did not find a relationship between colours and morphology, either, again finding the largest population of AGN in the green valley, with early-type AGN hosts peaking

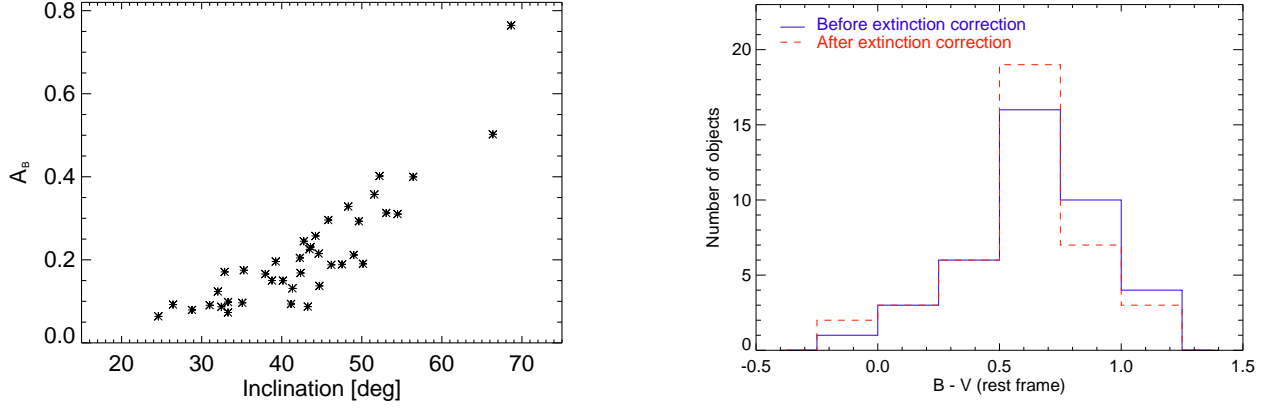


Fig. 12. *Left:* Relationship between the extinction A_B measured in B band and inclination for late-type AGN host galaxies in the SXDS field. *Right:* Histogram showing the distribution of $B - V$ colour before (solid blue line) and after (dashed red line) extinction correction for late-type AGN host galaxies selected in the SXDS field.

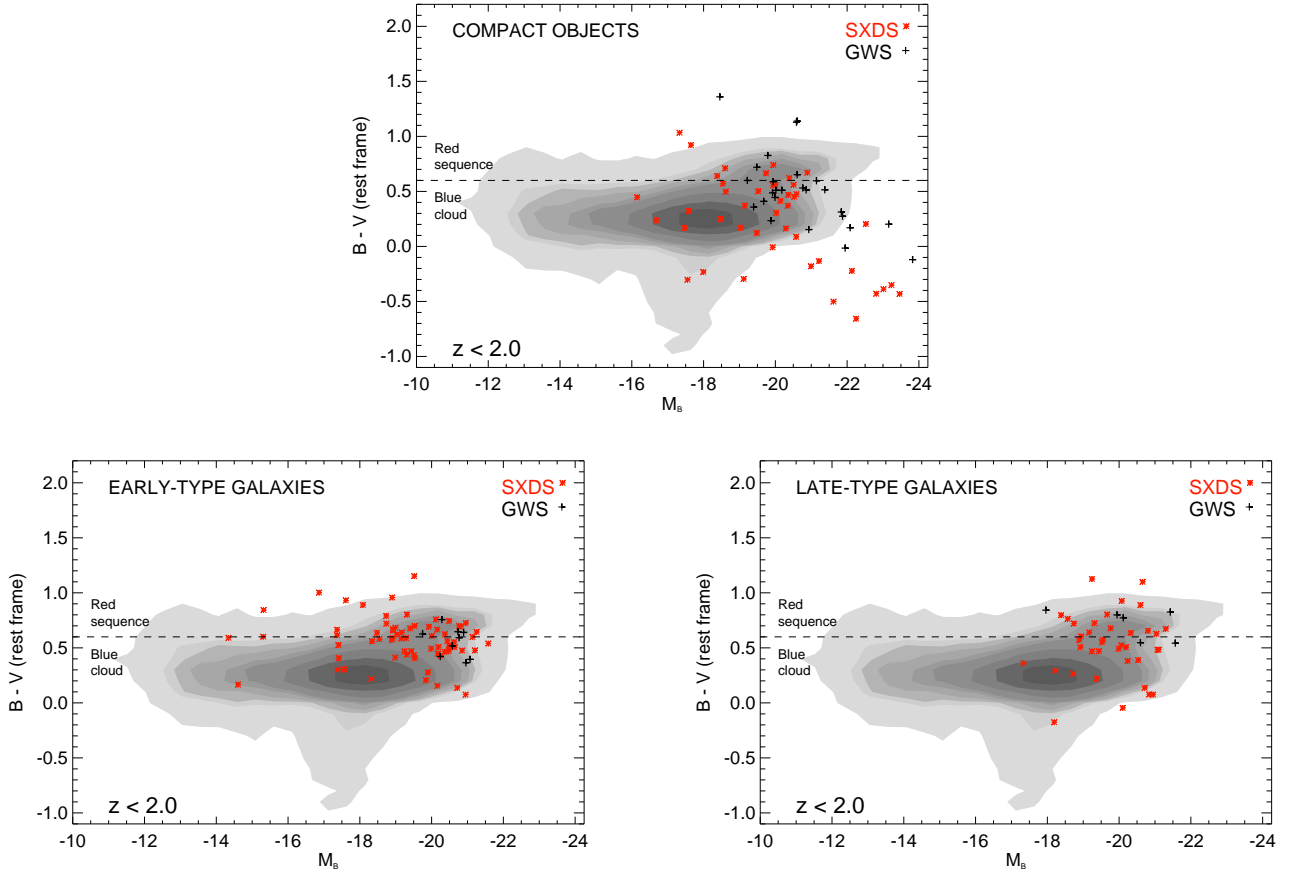


Fig. 14. Colour-magnitude diagram showing the relationship between the rest-frame $B - V$ colour and the absolute magnitude in the B band for different morphological types, using a sample of X-ray selected AGN in the SXDS (red stars) and GWS (black crosses) fields. All AGN having redshifts $z \leq 2.0$ are presented, compact (top), early- (bottom left) and late-type (bottom right) galaxy hosts. Morphological classification of active galaxies in the SXDS field is described in Section 3, while morphological classification of active galaxies in the GWS field is described in Pović et al. (2009a). The sample of AGN is compared with the sample of normal galaxies in the CDF-S field (Wolf et al. 2001, 2004, 2008) represented with contours. Grey scales of the contours are scaled to the data, where the darkest and brightest show the highest and the lowest density of the sources, respectively. The dashed line shows the Melbourne et al. (2007) separation between the galaxies belonging to the red sequence ($B - V > 0.6$) or to the blue cloud ($B - V < 0.6$).

below the red sequence, while the population of AGN in late-type galaxies peaks in the green valley, above the blue cloud population of similar masses. Moreover, Mainieri et al. (2011) studied the colours and morphology of Type-2 QSO at redshifts between 0.8 and 3 in the XMM-COSMOS field, and they found that most of their objects have rest-frame colours in the green valley, pointing out that this is the effect of a luminosity-selected rather than a mass selected sample. More than 80% of their objects have stellar masses above $10^{10} M_{\odot}$, mostly showing bulge-dominated morphologies, and weak signs of recent mergers or discs.

4.3. CMRs in relationship with X-ray type

In order to study the colour-magnitude diagrams in relation with X-ray obscuration, we have performed a coarse nuclear type classification based on a diagnostic diagram relating the X/O flux ratio and hardness ratio $HR(2 - 4.5keV/0.5 - 2keV)$. The X/O flux ratio has been shown to segregate efficiently between active and non-active/Compton-thick galaxies (Alexander et al. 2001; Fiore et al. 2003; Civano et al. 2007), while the hardness ratio $HR(2 - 4.5keV/0.5 - 2keV)$ is very sensitive to absorption, and thus capable of disentangling X-ray type-1 (unobscured or unabsorbed) from X-ray type-2 (obscured or absorbed) AGN (Mainieri et al. 2002; Della Ceca et al. 2004; Perola et al. 2004; Caccianiga et al. 2004; Dwelly et al. 2005; Hasinger 2008). Full details on the methodology applied are given in Pović et al. (2009a). According to this, all objects having $X/O > 0.1$ and $HR(2 - 4.5keV/0.5 - 2keV) < -0.35$ have been classified as X-ray type-1 AGN, while those with $X/O > 0.1$ and $HR(2 - 4.5keV/0.5 - 2keV) > -0.35$ have been catalogued as type-2 (obscured) nuclei. Those with $X/O < 0.1$ have been classified as Compton-thick/non-active galaxies. Figure 15 shows the described diagram of X-ray type classification. 52% and 39% of the total number of sources with optical counterparts have been classified as X-ray type-1 and type-2 AGN, respectively. The dashed-line box indicates the locus of the X-ray type-1 region according to Della Ceca et al. (2004). This box has been considered as the 'highest probability' region for finding X-ray unobscured AGN, and is populated by 51% of the X-ray type-1 objects. The remaining 10% are found in the region typical of Compton-thick/non-active galaxies.

Using the complete sample of objects, we have studied the relationship between the B - V rest-frame colour and the $HR(2 - 4.5keV/0.5 - 2keV)$ hardness ratio. Both X-ray type-1 and X-ray type-2 sources span the same range of B - V colour, and apparently there is no relationship between the observed optical and X-ray colours when the complete population of AGN is considered. However, performing the Kolmogorov-Smirnov analysis produces the result that the two distributions might be different, although the evidence is not conclusive, having a probability factor of 0.3.

Figure 16 shows the CMRs in relation with the X-ray obscuration. X-ray type-1 and type-2 sources have been represented from both the SXDS and GWS fields, and compared with the distribution of the complete sample of normal galaxies from the CDF-S field. As can be seen there is no clear separation between X-ray unobscured and obscured sources in the colour-magnitude diagram. We have studied this diagram in four redshift intervals (same intervals as in Figure 11), and have found no clear separation between X-ray type-1 and type-2 sources in any of them. We studied the X-ray obscuration for each morpho-

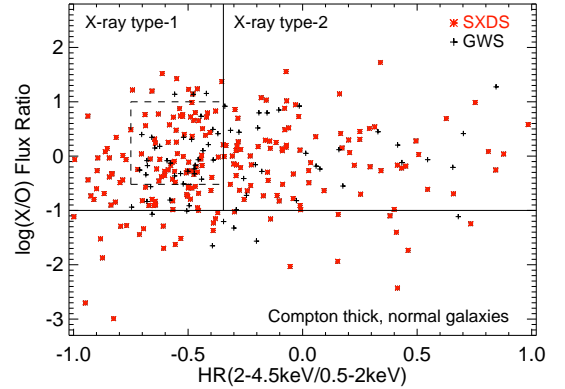


Fig. 15. Relationship between the X/O flux ratio and $HR(2 - 4.5keV/0.5 - 2keV)$ hardness ratio, for X-ray emitters with optical counterparts in the SXDS (red stars) and GWS (black crosses) fields. Solid lines separate X-ray type-1 (unobscured) and X-ray type-2 (obscured) regions and the area with $X/O < 0.1$, where Compton thick AGN, normal galaxies and stars can be found (e.g. Fiore et al. 2003). The dashed line box shows the limits obtained by Della Ceca et al. (2004) where $\sim 85\%$ of their spectroscopically identified AGN with broad emission lines have been found. In this work, $\sim 51\%$ of the X-ray type-1 sources are located inside this box.

logical type of our analysed sample. Almost all active galaxies (95%) detected as compact are unobscured sources in X-rays, with most of them (more than 80%) having blue B - V rest-frame colours. High luminosity QSO sources, being placed in the region devoid of normal galaxies, are found to be the most unobscured sources, having $HR(2 - 4.5keV/0.5 - 2keV) < -0.5$, while compared with them, compact sources belonging to the green valley and the blue cloud have lower X-ray obscuration ($-0.5 \leq HR(2 - 4.5keV/0.5 - 2keV) \leq -0.36$). On the other hand, when considering early- and late-type active galaxies, no relation has been found between the morphology and X-ray obscuration. Early- and late-type AGN in our sample hosts present a mixture of both X-ray unobscured and obscured sources. For both morphological types, $\approx 55\%$ of sources are unobscured, while the remaining $\approx 45\%$ are obscured. Moreover, there is no significant relationship between the X-ray obscuration and optical B - V rest-frame colour for both morphological types. 55% and 50% of unobscured and obscured early-type AGN are found to have blue optical colours, respectively, with very similar values for late-type hosts (58% and 50%). However, early-type galaxies that reside in the blue cloud are found to be more unobscured in X-rays ($-0.8 \leq HR(2 - 4.5keV/0.5 - 2keV) \leq -0.5$) compared with those belonging to the green valley ($HR(2 - 4.5keV/0.5 - 2keV) > -0.5$). This might suggest that part of the X-ray obscuration is due to the galaxy itself, moving the host-galaxy colours from blue cloud to red sequence. X-ray obscured early-type galaxies cover a wide range of hardness ratios (up to 1.0), with those sources belonging to the blue cloud and green valley having slightly lower obscuration compared to objects located in the red sequence. On the other hand, X-ray unobscured late-type sources seem to be more obscured than unobscured early-types, while for X-ray obscured late-types obscuration seems to be similar to that of obscured early-type galaxies.

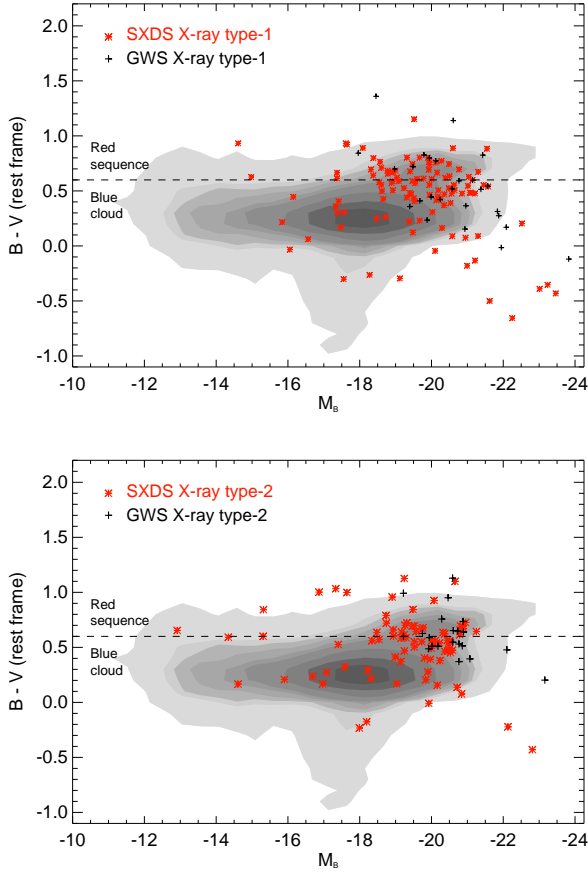


Fig. 16. Colour-magnitude diagram showing the relation between the rest-frame $B - V$ colour and the absolute magnitude in the B band for X-ray type-1 (unobscured; *top*) and X-ray type-2 (obscured; *bottom*) AGN, selected in the SXDS (red stars) and GWS (black crosses) fields. All sources with redshifts $z \leq 2.0$ have been represented. AGN sample has been compared with the sample of normal galaxies selected in the CDFS field (Wolf et al. 2001, 2004, 2008) represented with contours. The grey scales of the contours are scaled to the data, where the darkest and brightest show the highest and the lowest density of the sources, respectively. The dashed line shows the Melbourne et al. (2007) separation between the galaxies belonging to the red sequence ($B - V > 0.6$) or to the blue cloud ($B - V < 0.6$).

Recently, Pierce et al. (2010) studied the nuclear and outer $U - B$ colours in relationship with X-ray obscuration, through the hardness ratio $HR(2-7keV/0.5-2keV)$, using a sample of X-ray selected AGN in the AEGIS field at redshifts $0.2 < z < 1.2$. For most of their objects selected as X-ray type-1 AGN they obtained bluer colours, while for X-ray type-2 sources hosts are characterised by redder colours. As shown in Figure 16, no clear separation of such a type has been found between the $B - V$ colour and the $HR(2 - 4.5keV/0.5 - 2keV)$ hardness ratio used in this work, when the complete population of AGN is observed. However, as described above, when we segregate X-ray obscuration for different morphological types, it seems that there might be a certain correlation between X-ray and optical colours.

4.4. CMRs in relationship with X/O flux ratio

Finally, we studied the CMRs in relationship with the X-ray-to-optical (X/O) flux ratio. The physical explanation of this parameter is still not evident, but as suggested in Pović et al. (2009b) it might be related with the accretion rate. Studying X-ray properties, such as the X/O flux ratio and X-ray luminosities, we can test the black hole growth rate in relationship with properties of host galaxies, colours and morphology.

Figure 17 shows the CMRs according to the X/O flux ratio. We have studied the distribution of AGN analysed in this work, considering five ranges of X/O flux ratio. We have also represented a distribution of objects having very low X/O flux ratios ($\log X/O < -1$) characteristic of Compton thick sources and/or normal galaxies (e.g., Alexander et al. 2001; Fiore et al. 2003; Civano et al. 2007). As can be seen, most of these objects also reside in the green valley, having colours that correspond to most AGN sources.

Examining Figure 17, turns out that the distribution of AGN sources moves on the colour-magnitude diagram as the X/O flux ratio changes. Objects having higher values of the X/O flux ratio (e.g. $\log X/O > 0.5$) have bluer colours, while most AGN with lower X/O flux ratio have red and green colours with respect to that of normal galaxies. This might be related with two scenarios. First, that AGN with higher X/O flux ratio, have younger stellar populations, therefore showing bluer optical colours. In the case that the X/O flux ratio is a parameter proportional to the Eddington ratio, as suggested by Pović et al. (2009b), and if larger accretion rates and stronger AGN activity provoke a stronger AGN feedback, then this might be in contrast to the usual prediction that the AGN feedback quenches the star formation, unless we are observing the initial phases when star-formation quenching is just beginning. And second, in the case of very high Eddington ratios, AGN do contribute to the optical colours of their host galaxies, making them bluer. We can also notice that all sources located in the region not covered by normal galaxies, being very blue, very luminous, and probably high redshift QSO sources, have lower values of X/O flux ratio ($\approx \log X/O \leq 0$). Although the analysed sample of AGN seems to be representative of a full X-ray population as shown in Section 2.6, we should be aware that the observed trends represent just a small fraction of the full X-ray population.

Figure 18 shows the normalised distributions of X/O flux ratio for early- and late-type galaxies, and for X-ray unobscured and obscured sources of a sample analysed in this paper (see Section 2.6) and of all optical counterparts. It can be seen that high values of the X/O flux ratio ($X/O > 0.5$) correspond to AGN being hosted by later-types. This has already been obtained by Pović et al. (2009b), suggesting that late-type AGN, having more material to feed the black hole, have higher Eddington ratios compared with early-type AGN. Recently, Mainieri et al. (2011) obtained the same result for Type-2 QSOs, where disk-dominated or merging systems in their sample have higher accreting rates in comparison with bulge-dominated galaxies. Moreover, we compared the X-ray luminosities in three energy ranges, soft, hard, and veryhard (see Table 1) for early- and late-type active galaxies, as can be seen in Figure 19. Performing the Kolmogorov-Smirnov statistic, it was found that the distributions are different in the three ranges, being significantly different in hard and veryhard X-rays with probability factors of only 0.0004 and 0.025 that they belong to the same parent distribution. Again, it can be seen that AGN hosted by later-types show higher X-ray activity compared with early-types. On the other hand, when we observe X-ray luminosities with respect

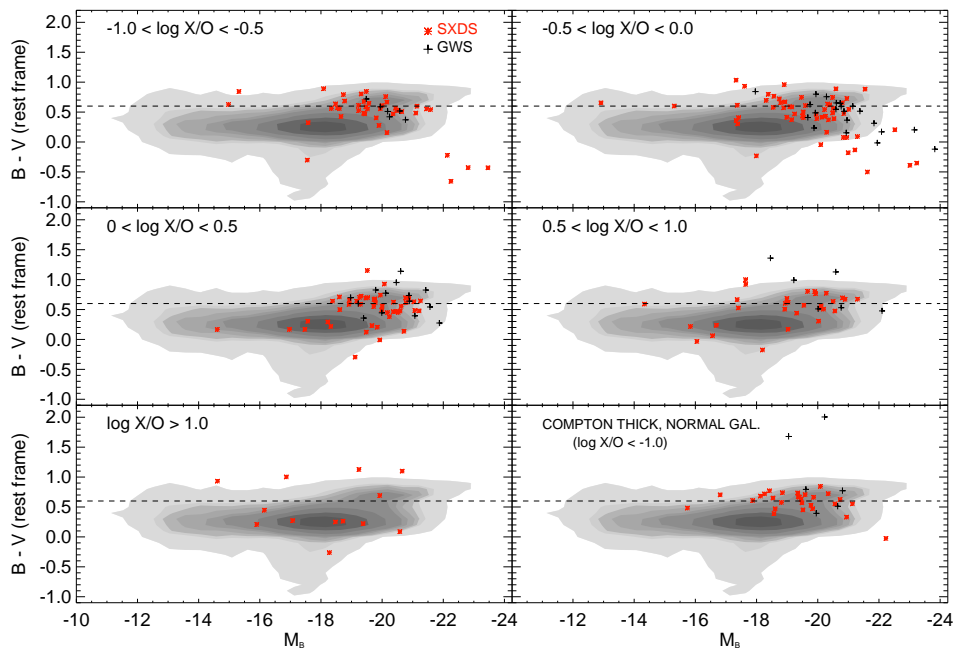


Fig. 17. Colour-magnitude diagram showing the relationship between the rest-frame $B - V$ colour and the absolute magnitude in the B band for AGN in the SXDS (stars) and GWS (crosses) fields having different X-ray-to-optical flux ratio. All sources have redshifts $z \leq 2.0$. The sample of AGN is compared with the sample of normal galaxies in the CDF-S field (Wolf et al. 2001, 2004, 2008) represented with contours. Grey scales of the contours are scaled to the data, where the darkest and brightest show the highest and the lowest density of the sources, respectively. The dashed line shows the Melbourne et al. (2007) limit between galaxies belonging to the red sequence ($B - V > 0.6$) and those in the blue cloud ($B - V < 0.6$). The bottom right diagram shows the distribution of objects classified as non-AGN (Compton thick and normal galaxies), having very low values of the X/O flux ratio.

to the $B - V$ colour, dividing all sources into red ($B - V > 0.6$) and blue ($B - V < 0.6$) active galaxies, the Kolmogorov-Smirnov analysis suggests that their X-ray activities are not significantly different, having probabilities of 93%, 68% and 81% in three energy ranges, respectively, and that they belong to the same parent distribution.

Finally, we compared the normalised distributions of X/O flux ratios for X-ray type-1 and type-2 AGN of a sample analysed in this paper (middle panel) and of all optical counterparts (bottom panel). We found similar distributions between two samples, where lower values of the X/O flux ratio (< 0) are more populated by X-ray unobscured AGN.

4.5. Summary: our results and current models of AGN formation and evolution

As shown in Figure 10, and analysed above, AGN hosts seem to have different colours as compared to normal galaxies, with the peak of red/blue AGN host galaxies being moved to bluer/redder colours, respectively. As mentioned in Section 4.2, in order to understand better what we see on the colour-magnitude diagrams and to relate the results obtained with the existing models of AGN formation and evolution, it is necessary to study colour-magnitude relations in more detail and instead of observing whole populations of active galaxies, to observe different morphological and nuclear types. As has been seen, almost all AGN classified as compact objects (possible QSO sources) are found to be X-ray unobscured and blue galaxies. However, when ob-

serving the two main morphological types, early- (which seem to be the majority of X-ray detected AGN) and late-type galaxies, no relationship has been found between colours and morphology, showing that early-/late-type X-ray selected AGN are not necessarily red/blue as non-active galaxies, respectively. In order to explain the presence of similar ('green') colours for both morphological types being located in the green valley, there might be two possibilities:

1) *Early- and late-type X-ray detected AGN have different stellar populations, similar to those of normal galaxies belonging to the red sequence and blue cloud, respectively.* In this case, two mechanisms could be responsible for the changing colours of AGN: AGN contribution, affecting more early-types and making them bluer, and dust reddening, affecting most of all late-types and making them redder. However, we still lack proof for this scenario. As shown in Section 4.1, AGN contribution to optical colours has shown to be negligible in most (if not all) previous analyses (Kauffmann et al. 2007; Nandra et al. 2007; Silverman et al. 2008; Cardamone et al. 2010), for at least 90% of AGN (Pierce et al. 2010). Moreover, we have seen that it is still not very clear how great the influence of the dust reddening effect could be on the optical colours (Cardamone et al. 2010; Xue et al. 2010). However, even if the dust-reddening effect is significant (moving later-types to bluer colours after extinction correction), since most AGN reside in early-type systems (being less affected by dust), after extinction correction most of AGN might still be residing in the green valley, without showing the colour bi-modality typical of non-active galaxies.

2) *Early- and late-type X-ray detected AGN have similar*

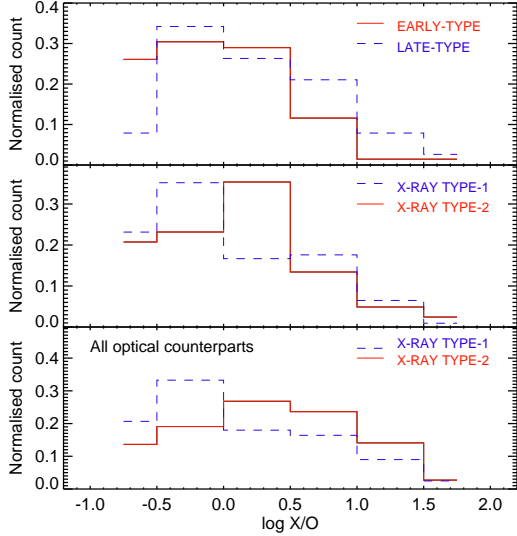


Fig. 18. Normalised X/O flux ratio distributions. (*Top*) Two main morphological types, early- (solid red line) and late-type (dashed blue line) active galaxies, are presented. The other two panels represent X-ray type-1 (dashed blue line) and type-2 (solid red line) sources of a sample analysed in this paper (*middle*) and of all optical counterparts (*bottom*).

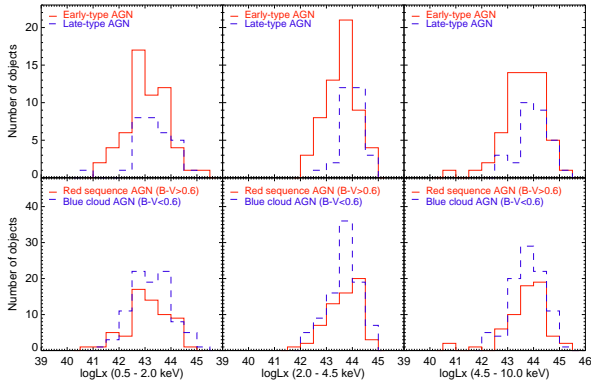


Fig. 19. From left to right: Histogram showing a distribution of X-ray luminosities in three energy ranges: soft (0.5–2.0 keV), hard-2 (2.0–4.5 keV), and very hard (4.5–10.0 keV), for *Top* Early- (solid red line) and late-type (dashed blue line) active galaxies, and *Bottom*: For red (solid red line) and blue (dashed blue line) AGN, having $B - V$ colours > 0.6 and < 0.6 , respectively.

stellar populations, different to those of normal galaxies belonging to the red sequence and blue cloud, respectively. AGN might be hosted by similar galaxies, being later early- and earlier late-type sources, presenting one phase in the evolution of galaxies. Moreover, in the redshift intervals studied in this work (see Figure 11), we have seen that most green valley AGN are found at redshifts $0.5 \leq z \leq 1.5$. This possibility could support the hypothesis that green valley AGN are transition objects, be-

tween the blue starburst galaxies and massive, red ellipticals, proposed already by various authors (e.g., Springel et al. 2005; Schawinski et al. 2006; Nandra et al. 2007; Georgakakis et al. 2008; Silverman et al. 2008; Treister et al. 2009).

We independently analysed three regions in the diagrams depending on their absolute magnitudes, and compared the results with the current models of AGN formation and evolution. Taking into account that no clear trend has been found on the CMR's when observing different morphological, X-ray, or X/O types, we should be cautious with them when studying galaxy evolution. As we move from the right to the left on the colour-magnitude diagrams (from higher to lower B band absolute magnitudes), we may interpret what we see in CMRs (Figures 10, 11, 14, 16, and 17) in the following way:

- *Region I:* Very high magnitudes ($M_B < -21.0$), very blue colours. This region corresponds to the one unpopulated by normal galaxies in our colour-magnitude diagrams. All AGN have high redshifts, from 1.5 to 2.0. They are all very blue, compact, and X-ray unobscured sources, having low values of hardness ratios. We may suspect that these sources are high-redshift quasars, and the AGN being in the so called 'QSO-mode' (Hopkins et al. 2005a,b; Springel et al. 2005; Croton et al. 2006; Hopkins et al. 2008a,b). In this mode, galaxy mergers and interactions are main mechanisms triggering nuclear activity in galaxies, providing enough material for both, star formation and supermassive black hole feeding. At the beginning the QSO is obscured by gas, but eventually it blows the obscuring and star-forming gas out from the galaxy through different AGN feedback mechanisms: ionisation, heating, radiation pressure (e.g., Ciotti & Ostriker 2007) and/or through strong winds and jets (e.g., Ciotti, Ostriker & Proga 2009; Shin, Ostriker & Ciotti 2010, and references therein). After that, the AGN can become unobscured, and the light coming from the nuclear region could dominate the light coming from the host galaxy.

- *Region II:* From intermediate to high magnitudes ($-21.0 < M_B < -18.0$), green colours. This is the region where $> 60\%$ of AGN from our sample are located, being mostly concentrated in the green valley, at the end of the blue cloud and at the bottom of the red sequence. As already mentioned and shown, the majority of X-ray detected AGN populate this region at redshifts $0.5 \leq z \leq 1.5$, showing different levels of nuclear activity (wide range of X/O flux ratio). The region is populated by compact sources, being again mostly unobscured and blue, but also by early- and late-type active galaxies, although AGN hosted by early-types are more numerous, as shown in Section 3. They have similar colours, and show similar levels of obscuration, being both unobscured and obscured in X-rays. It is possible that at these redshifts we are observing one of the peaks of nuclear activity in the evolution of galaxies (e.g., Hasinger, Miyaji & Schmidt 2005), related with the peak of starburst activity, with a possible dynamical delay (Davies et al. 2007; Schawinski et al. 2009; Wild, Heckman & Charlot 2010; Hopkins 2011). In order to explain the properties of the AGN observed in this region and in the redshift range considered, it seems that we need different mechanisms responsible for AGN fuelling. They include major and minor mergers (e.g., Surace et al. 2000; Springel et al. 2005; Di Matteo et al. 2005; Hopkins et al. 2005a,b; Cox et al. 2008; Hopkins et al. 2008a,b; Somerville et al. 2008), but also some secular mechanisms, such as minor interactions, disk instabilities, nuclear and large scale bars, colliding clouds, and supernovae explosions (e.g., Kormendy & Kennicutt 2004; Wada 2004; Hopkins & Hernquist 2009; Cisternas et al. 2011). Thus, it is not strange that most of the AGN we are observing are

hosted by early-type galaxies, being triggered through major/minor mergers. On the other hand, late-type AGN were probably triggered by some secular mechanisms, although recently it has been shown that in some cases discs can survive major mergers (Springel & Hernquist 2005; Robertson et al 2006; Governato et al. 2009). Therefore, what we are observing in this region are probably again AGN in the 'QSO-mode' (objects classified as compact), and phases of AGN activity before and after the 'QSO-mode', that we see as obscured and unobscured early- and late-type AGN, respectively, triggered as suggested above. An additional possibility for triggering at these redshifts could be also the 'radio-mode' accretion (Croton et al. 2006), active after the bright QSO phase, as a result of static hot halo formed around the host galaxy and the accretion of this hot gas on to a supermassive black hole. However, this mechanism is usually related with lower luminosities, and low accretion rates.

- *Region III*: Low optical magnitudes ($M_B > -18.0$), wide range of colours, from red to blue. Most AGN in this region are found at redshifts, $z \leq 1.0$. Around 30% of sources are compact, being normally blue and unobscured, while the remaining objects have been classified as early- or late-type galaxies, both unobscured and obscured in X-rays. What we observe in this region could be, on one side post 'QSO-mode' AGN, that we see as unobscured early- and late-type AGN, triggered by some of the mechanisms described above, including AGN with the 'radio-mode' accretion, and on the other side new triggered AGN, at these redshifts probably by some secular mechanisms (Cisternas et al. 2011, and references therein).

5. Conclusions

The main objective of this work was to study the connection between the AGN and the host galaxy, in order to derive clues for understanding some of the still unanswered fundamental questions related with the AGN fuelling mechanisms, and their formation and evolution. To achieve the proposed objectives, we studied morphology and colours, two key elements for analysing the properties of the host galaxies, in relation with X-ray properties describing the AGN activity (X-ray luminosities, X-ray obscuration, X/O flux ratio). We chose the SXDS field, observed in X-rays with XMM-Newton, which has one of the deepest optical data. After reducing X-ray data and after source detection, we derived a catalogue of 1121 X-ray emitters and cross-matched it with the publicly available optical catalogue. We obtained a catalogue of 808 X-ray emitters with optical counterparts, and for these sources we measured photometric redshifts and k-corrections, in order to obtain their rest-frame colours, absolute magnitudes, and luminosities. We obtained reliable photometric redshift information for 308 sources, for which we performed the analysis of their morphology and colours. We increased the SXDS sample by adding our previous data from the GWS fields.

The morphological classification still seems to be one of the main challenges, especially at high redshifts where obtaining reliable morphological information becomes very difficult. In this paper we used the galSVM (Huertas-Company et al. 2008, 2009) code, one of the new methods for morphological classification, especially useful when dealing with high redshift sources, and with the possibility of using a range of different morphological parameters and non-linear boundaries to separate different types. Moreover, we used SExtractor (Bertin & Arnouts 1996) in order to obtain the input parameters for galSVM execution, and the CLASS_STAR parameter, for separating between compact and extended sources. Using both galSVM and SExtractor, we obtained the following:

- A set of morphological parameters, including different parameters related with the concentration of the host galaxy light and its asymmetry.

- The final morphological classification, separating all AGN between compact sources and those hosted by one of the two main morphological types, namely early- and late-type galaxies. Approximately 22% of our objects have been classified as compact sources, while $\approx 30\%$ of the AGN have been estimated to be hosted by early-type, and $\approx 18\%$ by late-type galaxies. For about 23% of AGN, hosts were not very well resolved and the AGN might be residing in either early- or late-type galaxies, or experiencing possible interactions or mergers. Around 7% of AGN remained unidentified.

- Different problems, making morphological classification more difficult, have been recognised and tested in this paper. These include systematic trends of morphological parameters with source brightness, size, and redshift, low S/N ratios, and the number of parameters needed for the morphological classification. It has been seen that there is a trend of all observed morphological parameters with the apparent magnitude, size, and distance, and that parameters related with galaxy concentration (especially the M_{20} parameter compared with concentration index and/or Gini parameter) instead of with asymmetry seem to be the most affected. Moreover, it has been seen that the combination of two or three parameters is not enough to have a reliable morphological classification, as has been done with all previous non-parametric methods, and that classification in the multi-parameter space, with simultaneous use of different parameters and non-linear boundaries is needed.

- At redshifts $z \leq 2.0$, at least 50% of X-ray detected AGN analysed in this work are hosted by spheroids and/or bulge-dominated galaxies. However, at least 18% of AGN in our sample are hosted by late-types, suggesting that different mechanisms can be responsible for triggering the nuclear activity in galaxies.

We studied colours of X-ray selected AGN through colour-magnitude relations, comparing the AGN distribution with the typical distribution of normal galaxies. First, we used all types of active galaxies to analyse their redshift distributions (until $z \leq 2.0$). Second, using a high-redshift sample, we observed for CMRs in relation with morphology the first time, observing the distribution of active galaxies, belonging to different morphological types, on the colour-magnitude diagrams. Third, we studied the distribution of AGN on the colour-magnitude diagrams in relation with X-ray obscuration and, finally, in relation with X/O flux ratio. We conclude the following:

- Observing all types of X-ray detected AGN the highest number of sources is found to reside in the green valley, at the top of the blue cloud, and at the bottom of the red sequence, without showing any colour bi-modality typical for normal galaxies. AGN in our sample populate this region at redshifts $\approx 0.5 - 1.5$. However, a higher number of low luminosity AGN have been detected in this work, due to the high depth of the optical SXDS data in comparison with the most (if not all) previous surveys. This allows us to study the colour and morphological properties of these objects and to compare them with the properties of high luminosity AGN.

- More than 85% of objects classified as compact (possible QSO sources), are found to have blue optical colours and to be unobscured in X-rays. However, when observing the two main morphological types, no correlation has been found between the colours and morphology. The AGN studied in this work do not show the standard trend of normal galaxies, where early-types,

having older stellar populations, have redder colours, while late-type galaxies, being characterised with recent stellar formation have blue optical colours. AGN contribution and dust obscuration effects may affect the colours of early-/late-type galaxies moving them toward blue cloud/red sequence, respectively. However, additional work is still needed in order to quantify these contributions. On the other hand, even when mass-matched samples are used, no clear bi-modality has been seen in the optical colours. Moreover, both early- and late-type AGN are found to have similar ranges of X-ray obscuration, being both unobscured and obscured in X-rays.

Our findings confirm some previous suggestions that X-ray selected AGN residing in the green valley probably represent the transition population, quenching star formation and evolving to red sequence galaxies. What we might observe in the green valley is one of the peaks of AGN activity, with major and minor mergers probably being main triggering mechanisms, but also with the possibility of having some of the secular mechanisms responsible for fuelling. We observe AGN in the 'QSO-mode' (being compact, blue, and unobscured in X-rays) and different phases before (seeing them as obscured in X-rays) and after (seeing them as unobscured in X-rays) the 'QSO-mode', with AGN being hosted by later early- (the majority of sources) and earlier late-type galaxies, with similar stellar populations.

We would like to stress again that although a sample analysed in this paper seems to be representative of a full sample of X-ray population, all results presented here have been obtained for a sample of 25% of the full population.

Finally, the paper provides the scientific community with a catalogue of a large sample of AGN with the X-ray and optical data obtained in this work, including final morphological classification, all derived morphological parameters, rest-frame colours, and photometric redshifts. The complete catalogue of all 1121 X-ray sources, 808 optical counterparts, and the objects analysed in this paper is available in the electronic version of this paper, while the description of columns and the small example for seven objects are presented in the Appendix.

Acknowledgements. We thank the anonymous referee for a detailed analysis of the paper and constructive comments. We also thank Isabel Márquez Pérez, Josefa Masegosa Gallego, Jack Sulentic, and Ascensión del Olmo Orozco for long and very useful discussions. This work was supported by the Spanish *Plan Nacional de Astronomía y Astrofísica* under grant AYA2011-29517-C03-01. JIGS acknowledges financial support from the Spanish Ministry of Science and Innovation under project AYA2008-06311-C02-02. MP acknowledges Junta de Andalucía and Spanish Ministry of Science and Innovation through projects PO8-TIC-03531 and AYA2010-15169. We thank the SXDS, CDF-S, and COMBO-17 teams for making their data available to the astronomical community. We acknowledge support from the Faculty of the European Space Astronomy Centre (ESAC). We thank XMM-Newton Helpdesk for their helpful comments during the X-ray data reduction. This research has made use of software provided by the XMM-Newton Science Operations Centre and Chandra X-ray Center (CXC) in the application packages SAS and CIAO, respectively. IRAF is distributed by the National Optical Astronomy Observatory, which is operated by the Association of Universities for Research in Astronomy (AURA) under cooperative agreement with the National Science Foundation. This publication makes use of data products from the Two Micron All Sky Survey, which is a joint project of the University of Massachusetts and the Infrared Processing and Analysis Center California Institute of Technology, funded by the National Aeronautics and Space Administration and the National Science Foundation.

References

- Abraham, R. G., et al. 1996, *ApJ*, 107, 1
 Abraham, R. G., et al. 2003, *ApJ*, 588, 218
 Adams, T. F. 1977, *ApJS*, 33, 19
 Alexander, D. M., et al. 2001, *AJ*, 122, 2156
 Alonso-Herrero, A., et al. 2008, *ApJ*, 677, 127
 Aretxaga, I., et al. 2007, *MNRAS*, 379, 1571
 Baldry, I.K., et al. 2004, *ApJ*, 600, 681
 Barcons, X., et al. 2007, *A&A*, 476, 1191
 Barger, A.J., et al. 2003, *AJ*, 126, 632
 Barnes J. E. & Hernquist L., 1996, *ApJ*, 471, 115
 Bershad, M. A., Jangren, A., & Conselice, C. J., et al. 2000, *AJ*, 119, 2645
 Bertin, E. & Arnouts, S., 1996, *A&AS*, 117, 393
 Blanton, M. R., et al. 2007, *AJ*133, 734
 Blanton, M. R., et al. 2001, *AJ*121, 2358
 Bolzonella, M., Miralles, J. M., Pelló, R., 2000, *A&A*, 363, 476
 Brusa, M., et al. 2009, *A&A*, 507, 1277
 Caccianiga, A., et al. 2004, *A&A*, 416, 901
 Calzetti, D., et al. 2000, *ApJ*, 533, 682
 Cardamone, C. N., et al. 2010, *ApJ*, 721, L38
 Cepa, J., et al. 2011, *hsa6.conf.*, 167
 Cepa, J., et al. 2008, *A&A*, 490, 1
 Cepa, J., et al. 2007, *Rev. Mex. de Astronomía y Astrofísica Conference Series*, 29, 168
 Ciotti, L. & Ostriker, J. P. 2007, *ApJ*, 665, 1038
 Ciotti, L., Ostriker, J. P. & Proga, D. 2009, *ApJ*, 699, 89
 Cirasuolo, M., Magliocchetti, M. & Celotti, A. 2005, *MNRAS*, 357, 1267
 Cisternas, M., et al. 2011, *ApJ*, 726, 57
 Civano, F., et al. 2007, *A&A*, 476.1223C
 Choi, Y.-Y., et al. 2009, *ApJ*, 699, 1679
 Conselice, C. J., et al. 2003, *AJ*, 126, 1183
 Cox, T. J., et al. 2008, *MNRAS*, 384, 386
 Croton, D. J., et al. 2006, *MNRAS*, 365, 11
 Davies, R. I., et al. 2007, *ApJ*, 671, 1388
 Davis, M., et al. 2007, *ApJ*, 660, 1
 Della Ceca, R., et al. 2004, *A&A*, 428, 383
 Dickey, J. M. & Lockman, F. J., 1990, *ARRA&A*, 28, 215
 Di Matteo, T., et al. 2005, *Nature*, 433, 604
 Dwelly, T. et al. 2005, *MNRAS*, 360, 1426
 De Ruiter, H. R., Willis, A. G. & Arp, H. C. 1977, *A&AS*, 28, 211
 Feldmann, R., et al. 2006, *MNRAS*, 372, 564
 Fernández Lorenzo, M., et al. 2010, *A&A*, 521A, 27
 Ferrarese, L. 2004, in "Supermassive Black Holes in the Distant Universe", ed. Barger, A. (Netherlands: Kluwer Academic Publishers), 1
 Ferrarese, L. & Merrit, D. 2000, *ApJ*, 539, L9
 Fiore, F., et al. 2003, *A&A*, 409, 79
 Furusawa, H., et al. 2008, *ApJS*, 176, 1
 Gabor, J. M., et al. 2009, *ApJ*, 691, 705
 Gebhardt, K. et al. 2000, *ApJ*, 539, L13
 Georgakakis, A., et al. 2009, *MNRAS*, 397, 623
 Georgakakis, A. et al. 2008, *MNRAS*, 385, 2049
 Georgakakis, A. et al. 2007, *ApJ*, 660, L15
 Governato, F. et al. 2009, *MNRAS*, 398, 312
 Graham, A. W., Trujillo, I. & Caon, N. 2001, *AJ*, 122, 1707
 Griffith, R. L., & Stern, D. 2010, *AJ*, 140, 533
 Grogin, N. A., et al. 2005, *ApJ*, 627, 97
 Hasinger, G. 2008, *A&A*, 490, 905
 Hasinger, G. et al. 2007, *ApJS*, 172, 29
 Hasinger, G., Miyaji, T. & Schmidt, M. 2005, *A&A*, 441, 417
 Heckman, T. M. 1978, *PASP*, 106, 113
 Hewett, P. C., et al. 2006, *MNRAS*, 367, 454
 Hickox, R. C., et al. 2009, *ApJ*, 696, 891
 Ho, L. C., Filippenko, A. V., & Sargent, W. L. 1995, *ApJS*, 98, 477
 Hodgkin, S. T., et al. 2009, *MNRAS*, 394, 675
 Hopkins, P. F., 2011, *arXiv:astro-ph/1101.4230*
 Hopkins, P. F., & Hernquist, L. 2009, *ApJ*, 694, 599
 Hopkins, P. F., et al. 2008a, *ApJS*, 175, 356
 Hopkins, P. F. 2008b, *ApJS*, 175, 390
 Hopkins, P. F., et al. 2005a, *ApJ*, 630, 705
 Hopkins, P. F., et al. 2005b, *ApJ*, 625, L71
 Huertas-Company, M. et al., 2009, *A&A*, 497, 743
 Huertas-Company, M. et al., 2008, *A&A*, 478, 971
 Kauffmann, G. et al. 2007, *ApJS*, 173, 357

Kauffmann, G. et al. 2003, MNRAS, 346, 1055
 Kent, S. M., 1985, ApJS, 59, 115
 Kormendy, J. & Kennicutt, Jr. R. C. 2004, ARA&A, 42, 603
 Kormendy, J. & Richstone, D. 1995, ARA&A, 33, 581
 Lara-López, M. A. et al. 2011, PASP, 123, 252
 Lawrence, A. et al. 2007, MNRAS, 379, 1599
 Lotz, J. M., et al. 2004, AJ, 128, 163
 Magorrian, J. et al. 1998, AJ, 115, 2285
 Mainieri, V. et al. 2011, A&A, 535, 80
 Mainieri, V. et al. 2002, A&A, 393, 425
 Marconi, A. & Hunt, L. K. 2003, ApJ, 589, L21
 Mateos, S., et al. 2005, A&A, 444, 79
 McLure, R. J., Dunlop, J. S., & Kukula, M. J. 2000, MNRAS, 318, 693
 Melbourne, J. et al. 2007, ApJ, 660, 81
 Menanteau, F. et al. 2006
 Mortier, A.M.J. et al. 2005, MNRAS, 363, 563
 Nandra, K., et al. 2007, ApJ, 660, L11
 Peng, C. J., et al. 2006a, ApJ, 640, 114
 Peng, C. J., et al. 2006b, ApJ, 649, 616
 Perola, G. C., et al. A&A, 421, 491
 Pierce, C. M., et al. 2010, MNRAS, 408, 139
 Pierce, C. M., et al. 2007, ApJ, 660, L19
 Polletta, M. et al. 2007, ApJ, 663, 81
 Pović, M. et al. 2009a, ApJ, 706, 810
 Pović, M. et al. 2009b, ApJ, 702, L51
 Reach, W.T. et al. 2005, PASP, 117, 978
 Robertson, B. et al. 2006, ApJ, 645, 986
 Sánchez, S.F., et al. 2004, ApJ, 614, 586
 Scarlata, C. et al. 2006, arXiv:astro-ph/11644S
 Schawinski, K. et al. 2010, ApJ, 711, 284
 Schawinski, K. et al. 2009, ApJ, 692, L19
 Schawinski, K. et al. 2006, Nature, 442, 888
 Scoville, N. et al. 2007, ApJS, 172, 1
 Sekiguchi, K. et al., in preparation
 Shin, M. -S., Ostriker, J. P. & Ciotti, L. 2010, ApJ, 711, 268
 Silverman, J. D., et al. 2008, ApJ, 675, 1025
 Silverman, J. D., et al. 2005, ApJ, 618, 123
 Simpson, C. et al. 2006, MNRAS, 372, 741
 Somerville, R. S., et al. 2008, MNRAS, 391, 481
 Springel, V. et al. 2005, Nature, 435, 629
 Springel V., & Hernquist L. 2005, ApJ, 622, L9
 Steffen, A.T. et al. 2006, AJ, 131, 2826
 Strüder, L. et al. 2001, A&A, 365, L18
 Surace, J. A., et al. 2005, DR2 paper draft
 (http://swire.ipac.caltech.edu/swire/astronomers/data_access.html)
 Surace, J. A., et al. 2000, ApJ, 529, 170
 Sutherland, W., & Saunders, W. 1992, MNRAS, 259, 413
 Tasca, L.A.M., & White, S.D.M. 2011, A&A, 530, 106
 Taylor, M. B. 2005, ASPC, 347, 29
 Treister, E., et al. 2009, ApJ, 693, 1713
 tully, R. B., et al. 1998, AJ, 115, 2264
 Turner, M. J. L., et al. 2001, A&A, 365, L27
 Vapnik, V. 1995, "The Nature of statistical Learning Theory",
 (Springer-Verlag), 536
 Ueda, Y., et al. 2008, ApJS, 179, 124
 Wada, K. 2004, Coevolution of Black Holes and Galaxies, 186
 Warren, S.J. et al. 2007, arXiv:astro-ph/3037
 Weiner, B.J. et al. 2005, ApJ, 620, 595
 Wild, V., Heckman, T. & Charlot, S. 2010, MNRAS, 405, 933
 Wolf, C., et al. 2008, A&A, 492, 933
 Wolf, C., et al. 2004, A&A, 421, 913
 Wolf, C., et al. 2001, A&A, 377, 442
 Xue, Y. Q., et al. 2010, ApJ, 720, 368
 Younes, G., et al. 2011, arXiv:astro-ph/1104.4891

Appendix A: The catalogue

The full catalogue of data obtained in this work will be available in the electronic edition of this paper. The catalogue con-

tains SXDS X-ray data for all 1121 detected objects, optical identifications for the 808 sources, and measured morphological parameters, final morphological classification, redshifts, and rest-frame colours for 308 X-ray emitters with optical counterparts described in Section 2.6. Table A.1 shows an example of the format and content of the catalogue. The column entries are as follows:

Column 1 (ID): Identification number

Columns 2 and 3 (RA_x , DEC_x): Equinox J2000.0 right ascension and declination in degrees of the centroid in the X-ray catalogue.

Column 4 (F_s): X-ray flux in the soft (0.5 - 2 keV) band in $10^{-15} \text{ erg s}^{-1} \text{ cm}^{-2}$

Column 5 (F_h): X-ray flux in the hard (2 - 4.5 keV) band in $10^{-15} \text{ erg s}^{-1} \text{ cm}^{-2}$

Column 6 (F_{vh}): X-ray flux in the hard (4.5 - 10 keV) band in $10^{-15} \text{ erg s}^{-1} \text{ cm}^{-2}$

Column 7 (F_{tot}): X-ray flux in the hard (0.5 - 10 keV) band in $10^{-15} \text{ erg s}^{-1} \text{ cm}^{-2}$

Column 8 (F_{vh2}): X-ray flux in the hard (4.0 - 7 keV) band in $10^{-15} \text{ erg s}^{-1} \text{ cm}^{-2}$

Column 9 (F_{tot2}): X-ray flux in the hard (0.5 - 7 keV) band in $10^{-15} \text{ erg s}^{-1} \text{ cm}^{-2}$

Column 10 (SXDS.ID): Object name in the SXDS optical catalogue (Furusawa et al. 2008)

Columns 11 and 12 (RA_o , DEC_o): Equinox J2000.0 right ascension and declination in degrees. These coordinates correspond to the centroid in the broadband optical catalogue obtained by the SXDS team (see Section 2)

Columns 13 and 14 (R_c , R_{c_err}): R_c apparent magnitude and its error

Columns 15 and 16 (zphot, zphot_err): photometric redshift and its error (see Section 2.6)

Columns 17 and 18 (MabsB, MabsB_err): Absolute magnitude in B band and its error (see Section 4.1)

Columns 19 and 20 (B - V, B - V_err): Rest-frame B - V colour and its error (see Section 4.1)

Columns 21 and 22 (X/O, X/O_err): X-ray-to-optical flux ratio, computed as the ratio of the observed X-ray flux in the 0.5 - 4.5 keV energy range and optical flux in R_c band, and its error

Columns 23 and 24 (HR, HR_err): (2-4.5/0.5-2 keV) hardness ratio and its error (see Section 2)

Column 25 (Stellarity): SExtractor CLASS_STAR parameter. Column objects assigned as compact are all objects with this parameter ≥ 0.9 (see Section 3.1)

Column 26 (Elong): Elongation parameter obtained by SExtractor (Bertin & Arnouts 1996)

Column 27 (MSB): Mean Surface Brightness of the source, measured by galSVM (Huertas-Company et al. 2008)

Column 28 (A): Asymmetry index measured by galSVM, defined as in Abraham et al. (1996)

Column 29 (C): Abraham concentration index, measured by galSVM and defined as the ratio between the integrated flux within certain radius defined by the normalized radius = 0.3, and the total flux (Abraham et al. 1996)

Column 30 (Gini): Gini coefficient measured by galSVM and defined as in Abraham et al. (2003)

Column 31 (S): Smoothness of the source, measured by galSVM and defined as in Conselice et al. (2003)

Column 32 (M_{20}): Moment of light M_{20} , measured by galSVM and defined as in Lotz et al. (2004)

Columns 33 and 34 (p_1 , p_2): Probability that the galaxy belongs to early- or late-type, respectively (see Section 3.2)

Table A.1. Catalogue presenting morphological properties, colours, and photometric redshifts of X–ray emitters with optical counterparts in the SXDS field. In the electronic edition each object is represented per one line.

ID	RA_x	DEC_x	F_s	F_h	F_{vh}	F_{tot}	F_{vh2}	F_{tot2}
SXDS_ID	RA_o	DEC_o	R_c	R_{c_err}	z_{phot}	z_{phot_err}	MabsB	MabsB_err
B – V	B – V_err	X/O	X/O_err	HR	HR_err	Stellarity	Elong	MSB
A	C	Gini	S	M₂₀	p₁	p₂		
1	34.2059326	-4.9195004	0.3803	2.959	5.493	2.842	11.63	3.617
SXDS-iC-121387	34.20587083	-4.918922	23.745	0.012	1.89	0.09	-20.840	0.0111
0.077	0.021	0.635	0.316	0.295	0.561	0.03	1.349	26.994
0.098	0.450	0.690	0.039	-1.293	0.167	0.833		
2	34.2367325	-4.7958641	5.128	18.22	17.888	20.502	38.996	25.817
SXDS-iC-1616	34.23629167	-4.796003	22.373	0.004	0.615	0.004	-19.264	0.003
0.701	0.0150	1.255	0.198	-0.089	0.131	0.04	1.178	24.827
0.072	0.488	0.757	0.052	-1.964	0.703	0.297		
3	34.3014336	-4.8216581	1.458	2.807	5.575	5.763	12.206	7.190
SXDS-iC-157690	34.30122083	-4.821953	24.704	0.021	1.02	0.01	-19.291	0.009
0.588	0.047	1.960	0.904	-0.163	0.406	0.58	1.829	26.736
0.093	0.449	0.719	0.063	-1.664	0.908	0.092		
4	34.3149796	-5.0099578	2.910	2.602	2.188	6.941	0.0	8.819
SXDS-iC-086715	34.31469167	-5.010572	22.232	0.003	1.42	0.01	-22.251	0.005
-0.657	0.009	0.260	0.077	-0.499	0.228	0.97	1.071	25.493
0.120	0.538	0.822	-0.0	-1.523	0.989	0.011		
5	34.3232346	-4.9310899	1.083	4.228	2.751	3.707	8.398	5.0123
SXDS-iC-115045	34.3228583	-4.931603	21.780	0.003	0.845	0.007	-20.484	0.003
0.5301	0.007	0.165	0.0544	-0.041	0.292	0.03	1.325	25.331
-0.005	0.501	0.760	-0.153	-1.919	0.711	0.289		